The Astronomical Journal, 161:52 (24pp), 2021 February https://doi.org/10.3847/1538-3881/abcaa2

SDSS-IV MaNGA: Modeling the Spectral Line-spread Function to Subpercent Accuracy

David R. Law[1], Kyle B. Westfall[2], Matthew A. Bershady[3,4,5], Michele Cappellari[6], Renbin Yan[7], Francesco Belfiore[8], Dmitry Bizyaev[9], Joel R. Brownstein[10], Yanping Chen[11], Brian Cherinka[1], Niv Drory[12], Daniel Lazarz[7], and Shravan Shetty[3,13]

[1] Space Telescope Science Institute, 3700 San Martin Drive, Baltimore, MD 21218, USA; dlaw@stsci.edu
[2] University of California Observatories, University of California, Santa Cruz, 1156 High Street, Santa Cruz, CA 95064, USA
[3] University of Wisconsin—Madison, Department of Astronomy, 475 N. Charter Street, Madison, WI 53706-1582, USA
[4] South African Astronomical Observatory, PO Box 9, Observatory 7935, Cape Town, South Africa
[5] Department of Astronomy, University of Cape Town, Private Bag X3, Rondebosch 7701, South Africa
[6] Sub-department of Astrophysics, Department of Physics, University of Oxford, Denys Wilkinson Building, Keble Road, Oxford OX1 3RH, UK
[7] Department of Physics and Astronomy, University of Kentucky, 505 Rose Street, Lexington, KY 40506-0057, USA
[8] INAF—Osservatorio Astrofisico di Arcetri, Largo E. Fermi 5, I-50157, Firenze, Italy
[9] Apache Point Observatory, P.O. Box 59, Sunspot, NM 88349, USA
[10] University of Utah, Department of Physics and Astronomy, 115 S. 1400 E., Salt Lake City, UT 84112, USA
[11] New York University Abu Dhabi, P.O. Box 129188, Abu Dhabi, UAE
[12] McDonald Observatory, The University of Texas at Austin, 2515 Speedway, Stop C1402, Austin, TX 78712, USA
[13] Kavli Institute for Astronomy and Astrophysics, Peking University, Beijing 100871, People's Republic of China
Received 2020 August 31; revised 2020 November 13; accepted 2020 November 13; published 2021 January 6

Abstract

The Sloan Digital Sky Survey IV Mapping Nearby Galaxies at APO (MaNGA) program has been operating from 2014 to 2020, and has now observed a sample of 9269 galaxies in the low redshift universe ($z \sim 0.05$) with integral-field spectroscopy. With rest-optical ($\lambda\lambda 0.36$–$1.0\,\mu$m) spectral resolution $R \sim 2000$ the instrumental spectral line-spread function (LSF) typically has 1σ width of about 70 km s^{-1}, which poses a challenge for the study of the typically 20–30 km s^{-1} velocity dispersion of the ionized gas in present-day disk galaxies. In this contribution, we present a major revision of the MaNGA data pipeline architecture, focusing particularly on a variety of factors impacting the effective LSF (e.g., under-sampling, spectral rectification, and data cube construction). Through comparison with external assessments of the MaNGA data provided by substantially higher-resolution $R \sim 10{,}000$ instruments, we demonstrate that the revised MPL-10 pipeline measures the instrumental LSF sufficiently accurately ($\leqslant$0.6% systematic, 2% random around the wavelength of Hα) that it enables reliable measurements of astrophysical velocity dispersions $\sigma_{\rm H\alpha} \sim 20$ km s^{-1} for spaxels with emission lines detected at signal-to-noise ratio > 50. Velocity dispersions derived from [O II], Hβ, [O III], [N II], and [S II] are consistent with those derived from Hα to within about 2% at $\sigma_{\rm H\alpha} > 30$ km s^{-1}. Although the impact of these changes to the estimated LSF will be minimal at velocity dispersions greater than about 100 km s^{-1}, scientific results from previous data releases that are based on dispersions far below the instrumental resolution should be reevaluated.

Unified Astronomy Thesaurus concepts: Spectroscopy (1558); Galaxy kinematics (602); Astronomy data analysis (1858)

1. Introduction

The design of astrophysical instruments is always a trade-off between various competing factors. With limited detector real estate, there is an inherent tension between (i) the number of spectra that can be observed, (ii) the wavelength range that they can cover, and (iii) the spectral resolution (or the effective information content per wavelength).

The first is obviously attractive; the more spectra that can be observed simultaneously, the faster any survey can be completed, or the larger its eventual sample of objects. The second is similarly obvious; the rest-optical and NIR wavelength range is replete with a wealth of spectral features encoding information about the kinematics, stellar populations, chemical abundances, and sources of ionizing radiation. For the Sloan Digital Sky Survey (SDSS)-IV Mapping Nearby Galaxies at APO (MaNGA) survey for instance (Bundy et al. 2015; Blanton et al. 2017), the design of the instrument has allowed the survey to observe a sample of 10,000 galaxies with integral field unit (IFU) spectroscopy (roughly a factor ~10 larger than previous such surveys), at the same time as spanning a wide and contiguous wavelength range from 3600 to 10300 Å. This wavelength range crucially includes classic strong-line emission features from [O II] λ3727 to [S III] λ9531 that can characterize the mechanisms of ongoing star formation, stellar absorption features such as the Mg triplet at 5170 Å and the Ca triplet at 8550 Å that characterize the evolved population, and faint indices such as Na I at 8120 Å and FeH at 9916 Å that are sensitive to the initial mass function (e.g., Conroy & van Dokkum 2012; Parikh et al. 2018).

At the same time, high spectral resolution is critical to both separate spectral features that are close together in wavelength (e.g., the [O II] 3727 doublet) and to study the range of velocities present in gas or stellar populations along a given line of sight. Given the necessity of high spectral resolution in studies of galaxy kinematics, IFU surveys such as the Sydney-AAO Multi-object Integral field spectrograph survey (SAMI; Croom et al. 2012; Allen et al. 2015) have opted to trade spectral coverage for higher spectral resolution $R \sim 4500$ around key diagnostic features such as Hα. In contrast, at the spectral resolution of MaNGA ($R \sim 2000$), it is much more difficult to extract kinematic data as the astrophysical ionized-gas velocity dispersions are typically $\sigma_{\rm H\alpha} \sim 20$–$30$ km s^{-1} for

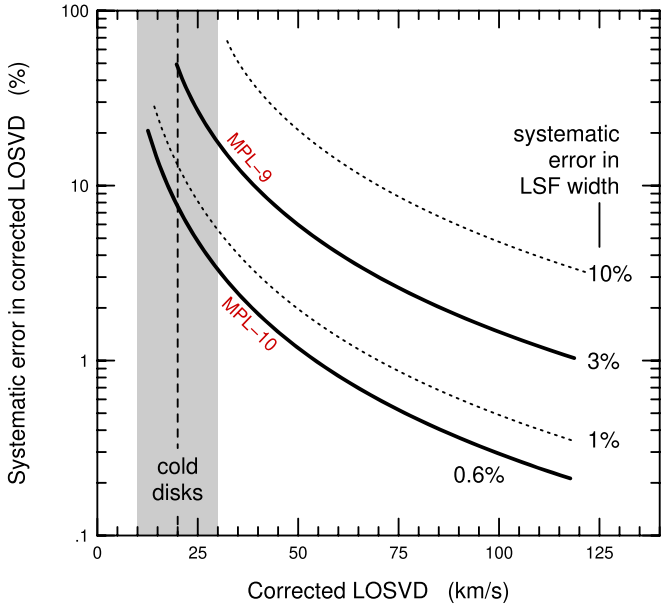

Figure 1. Systematic error in derived $\sigma_{H\alpha}$ as a function of $\sigma_{H\alpha}$ for various assumed errors in the MaNGA instrumental LSF. This is estimated analytically from the standard assumption that the instrumental and astrophysical dispersion add in quadrature. In order to achieve better than 10% accuracy in the regime of cold gas disks, the LSF must be known to better than 1%.

main-sequence star-forming galaxies. These astrophysical dispersions are dwarfed by the $\sim$70 km s^{-1} line widths produced by the instrumental line-spread function (LSF; i.e., the projection of the detector point-spread function onto the spectral axis).[14] Complicating matters further, MaNGA is a critically sampled ($\sim$2 pixels per FWHM) fiber-based instrument that feeds a pair of two-arm, Cassegrain-mounted spectrographs subject to varying gravitational flexure. As we show here, this leads to an instrumental LSF that is highly variable, spatially (from fiber to fiber), spectrally (both between arms and within each arm), and temporally.

To reliably recover astrophysical line widths on the order of 20 km s^{-1}, this instrumental contribution must be modeled in exquisite detail and accurately removed from the measured line widths (emphasizing that each of these requirements presents unique challenges). In this contribution, we present a major update to the original MaNGA data pipeline (Law et al. 2016) and demonstrate that the most recent MPL-10 survey data products meet (and indeed exceed) the 1% level of precision in the LSF necessary to study such astrophysical signals (see Figure 1).

This paper is organized as follows: In Section 2 we provide an overview of the MaNGA instrument and observing program, and highlight major changes that have been made to the data reduction pipeline (DRP) since the initial description by Law et al. (2016). In Section 3 we discuss the revised derivation of the instrumental LSF in the latest version of the MaNGA DRP (MPL-10; see Table 1), noting differences from earlier calibrations and publicly released data products. We describe changes that have been made to the MaNGA data analysis pipeline (DAP) since the earlier description by Westfall et al. (2019) in Section 4 and use internal tests to demonstrate the reliability of our estimates of the astrophysical gas and stellar velocity dispersions. We extend this discussion to consider the effects of beam smearing in Section 5. Finally, in Section 6 we compare the MaNGA data directly against independent external calibrators at much higher spectral resolution (up to $R \sim 11{,}000$) and demonstrate that the instrumental LSF estimates provided by the pipeline are accurate to better than 1% around the wavelength of Hα. We summarize our conclusions in Section 7.

Throughout our analysis we adopt a Chabrier (2003) stellar initial mass function and a ΛCDM cosmology in which $H_0 = 70$ km s^{-1} Mpc^{-1}, $\Omega_m = 0.27$, and $\Omega_\Lambda = 0.73$.

[14] For reference, a 20 km s^{-1} broadening of an $R = 2000$ LSF results in a 5% increase in the width of the observed line, whereas this same broadening results in a 22% increase at $R = 4500$.

Table 1
MaNGA Data Releases and Pipeline Versions

Version	Internal	External	Year	Galaxies[a]
3.1.1	MPL-11	DR17	2021	10010[b]
3.0.1	MPL-10	...	2020	9269
2.7.1	MPL-9	...	2019	7823
2.5.3	MPL-8	...	2018	6293
2.4.3	MPL-7	DR15	2018	4532
2.3.1	MPL-6	...	2017	4529
2.1.2	...	DR14	2017	2689
2.0.1	MPL-5	...	2016	2691
1.5.4	...	DR13	2016	1330
1.5.1	MPL-4	...	2015	1329
1.3.3	MPL-3	...	2015	624
1.1.2	MPL-2	...	2014	118
1.0.0	MPL-1	...	2014	58

Notes.
[a] Number of unique galaxy targets (discounting special Coma, M31, IC342, and globular cluster targets) with high-quality data cubes.
[b] Based on preliminary reductions of the final survey data.

2. Observational Data

The MaNGA hardware design is described in detail by Drory et al. (2015), and consists of 1423 optical fibers feeding the two BOSS spectrographs (Smee et al. 2013) installed at the Cassegrain focus of the Sloan Digital Sky Survey 2.5 m telescope at Apache Point Observatory (Gunn et al. 2006). Each of the six removable cartridges interfaces with a plugplate system, and contains a full complement of optical fibers bundled into hexagonal IFUs ranging in size from 19 to 127 fibers along with a set of 12 seven-fiber minibundles for photometric calibration (Yan et al. 2016) and 92 individual fibers used for sky subtraction. In each cartridge the fibers are permanently mounted in a series of v-groove blocks attached to two pseudo-slits that align with the BOSS spectrograph slitheads. Since BOSS is a dual-beam spectrograph, a dichroic beamsplitter divides the light into blue ($\lambda\lambda$3600–6300) and red ($\lambda\lambda$5900–10300) cameras. In order to mitigate the effects of atmospheric differential refraction on the effective sampling of the MaNGA fiber bundles (see Law et al. 2015), each plate is typically observed in sets of three 15-minute dithered exposures with similar seeing, transparency, and hour angle, and repeated as necessary on multiple MJDs (modified Julian dates) to reach a target effective depth.

The main MaNGA survey galaxies are drawn from a flat mass distribution in the range $M_* = 10^9$–$10^{11}\,M_\odot$, with subsamples reaching 1.5 and 2.5 effective radii and a "color-enhanced" subsample designed to obtain sampling of sparser regions of color–magnitude space (see discussion by Wake et al. 2017). Since its original conception as a dark-time galaxy survey

(Law et al. 2015; Yan et al. 2016), the MaNGA program has since grown to also encompass a variety of ancillary programs (e.g., observations of M31, IC342, and the Coma cluster) as well as a bright-time survey of a large library of stellar spectra (MaStar; Yan et al. 2019). The MaNGA DRP has thus also evolved substantially since the initial DR13 public data release (v1.5.4) described by Law et al. (2016) to accommodate both this new observing mode and a variety of improvements that have been made for the main galaxy program.

In brief, the DRP extracts individual fiber spectra from the four detectors via row-by-row optimal extraction, performs sky subtraction and flux calibration (Yan et al. 2016) using dedicated calibration fibers and fiber bundles, and resamples each calibrated spectrum onto a common wavelength grid. While the majority of these algorithms are identical between MaNGA and MaStar, some minor differences exist since the targets range over 20 magnitudes in brightness (from $g \sim 6$ for bright stellar library targets to $g \sim 26$ arcsec^{-2} for observations of intracluster light in the Coma cluster; Gu et al. 2018) and from dark-sky conditions to mere degrees away from the full moon. Additionally, for MaNGA galaxy observations, the DRP also combines the individual fiber spectra into a composite rectified data cube, while for MaStar stellar targets, the DRP extracts a composite 1D spectrum corrected for atmospheric differential refraction and geometric fiber-bundle losses from the individual fiber spectra. As discussed by Law et al. (2016), the DRP is written almost entirely in IDL, with some C bindings for runtime optimization.

In Table 1 we list the versions of the MaNGA pipeline data products available both internally to the SDSS collaboration (through MaNGA product launches, i.e., "MPL") and externally to the broader astronomical community (through data releases, i.e., "DR"). Some of the changes made for DR13, DR14, and DR15 have already been described by Albareti et al. (2017), Abolfathi et al. (2018), and Aguado et al. (2019), respectively. Compared to the DR13 pipeline described by Law et al. (2016), the major changes that have been made to the DRP include:

1. Visual yearly inspection of all IFU exposures failing comparisons against established SDSS broadband pre-imaging data. Identification and flagging of IFU frames affected by terrestrial satellite trails allow recovery of high-quality composite data cubes from many that were previously flagged as not of science quality.
2. More extensive identification and masking of foreground stars via Galaxy Zoo 3D (K. Masters et al. 2020, in preparation)
3. Production of composite single-object spectra for MaStar stellar library targets (v2.0.1), and de-redshifting of the resulting spectra (v2.3.1) to the stellar rest frame (see details given by Yan et al. 2019)
4. Inclusion of full spatial covariance matrices for the galaxy data cubes (v2.0.1).
5. Modification of straylight and bias routines to reduce systematics effects highlighted by ultra-deep observations for the Coma cluster ancillary program (Gu et al. 2018, 2020, v2.3.1)
6. Adoption of the BOSZ flux-calibration templates (Bohlin et al. 2017) instead of the Kurucz model atmospheres (Gray & Corbally 1994; v2.3.1; see Yan et al. 2019).
7. Adjustments to the IFU fiber-bundle metrology to compensate for a ∼2.5% scale error in laboratory measurements (v2.5.3, v2.7.1; see Section A).
8. Adoption of the Fitzpatrick (1999) extinction curve for standard star calibrations instead of the O'Donnell (1994) curve (v2.5.3).
9. Modification to handle short (5–300 s) exposures for bright MaStar targets (v2.5.3).
10. Addition of special processing to model, subtract, and flag data affected by a bright "blowtorch" artifact resulting from an electronics failure in the r1 detector during the final year of the survey (v2.7.1, v3.0.1; see Section B).
11. Substantial revisions to the spectral LSF estimation affecting the recovered galaxy velocity dispersions (see discussion in Section 3.6).

The most recent version of the MaNGA DRP data products (MPL-10) consists of all MaNGA and MaSTAR plates completed up to MJD 58933 (2020 March 25). As determined from the MPL-10 drpall summary file (drpall-v3_0_1.fits), it contains 10,529 data cubes corresponding to 630 plates, and 33,360 MaSTAR spectra (26618 unique stars) across 1534 plates. Of the 10,529 data cubes, 9556 represent galaxies (i.e., discounting the Coma, IC342, M31, and globular cluster ancillary programs and a few other non-galaxy special plates). A small number of these data cubes (162) are flagged by the pipeline as "DONOTUSE" for science based on significant differences between the MaNGA photometry and prior SDSS imaging. These differences can be due to, e.g., poor focus (in which an IFU partially fell out of the plate during observations), unmasked cosmic rays, satellite trails, supernovae, etc. Of the remaining 9394 galaxy data cubes, there are 9269 unique galaxies, roughly 100 of which have two or more independent observations.

The MaNGA MPL-10 data products are available internally to collaboration members both in flat FITS file form[15] and via a python-based API and web application[16] (Marvin; Cherinka et al. 2019). Similarly, DR15 data products are available publicly via the same sources.

3. Spectral LSF in the MaNGA DRP

In order to measure the astrophysical stellar or gas velocity dispersion, e.g., $\sigma_{\mathrm{H}\alpha}$ from the observed Hα emission-line profile in a given spaxel, it is critical to have accurate and precise knowledge of the spectral LSF (i.e., the projection into the wavelength domain of the detector point-spread function convolved with the top-hat pixel sampling). Since MaNGA uses spectrographs mounted at the Cassegrain focus of the SDSS 2.5 m telescope, the LSF modulates due to time-variable gravitational flexure in the fibers, camera optics, and detector focal plane; these temporal variations complicate efforts to obtain a robust LSF measurement.

In this section, we discuss the MPL-10 approach taken by the DRP to measure the initial LSF from calibration arc-lamp spectra (Section 3.1), account for pixel broadening (Section 3.2), adjust the measurements to match co-temporal night-sky features (Section 3.3), and account for spectral resampling (Section 3.4) and IFU cube building algorithms (Section 3.5). Overall

[15] http://www.sdss.org
[16] https://sas.sdss.org/marvin/

differences from the initial MaNGA data products provided in previous data releases are summarized in Section 3.6.

3.1. Arc-line Model

The spectral LSF of the MaNGA data is first estimated using 4 s observations of a Neon–Mercury–Cadmium arc-lamp spectrum taken at the beginning of each series of MaNGA observations of a given plate and roughly every 2 hr thereafter. This arc frame provides a well-populated series of bright unresolved emission lines spanning the wavelength range of the instrument. Since the wavelength zero-point is curved along the pseudo-slit (see, e.g., Figure 22 of Law et al. 2016), this means that a given arc line lies at a range of different "pixel phases" (i.e., centroid locations within a pixel) for different fibers, and as the relative fiber-to-fiber wavelength solution is accurate to better than 0.024 pixels rms (see Section 10.3 of Law et al. 2016), it is therefore possible to combine the observed spectra from multiple fibers to obtain a super-sampled realization of the arc-line profile.

As shown in Figure 2, these line profiles are well described by a simple Gaussian model for both the blue and red cameras across a wide range of wavelengths. While the residuals from the simple Gaussian fit show evidence for intrinsic kurtosis in the line profile (consistent with expectations for the convolution of a 2D Gaussian with the circular image of the optical fiber), the peak amplitude of this residual is sufficiently small ($\sim$5% relative to the peak intensity of the line) that it is expected to have a negligible effect on our analysis.[17] We therefore fully characterize the shape of the LSF by a single value ω[18] giving the 1σ width of a Gaussian profile fit to the observed pixel values (after first subtracting off the small continuum signal using the median in a 100-pixel window surrounding the line).

As illustrated by Figure 3, ω varies over each of the four detectors as a complicated function of both wavelength and fiberid along the pseudo-slit. Similarly, it can change from exposure to exposure with varying telescope/spectrograph focus, gravitational flexure, and changing observing conditions. The DRP therefore constructs a model of ω in pixel units using the individual arc lines in each calibration frame that will be used as the base calibration for nearby science exposures (the median science exposure is within 34 minutes of the nearest arc frame, 86% of exposures are within 1 hr, and 99.5% are within 2 hr).

First, we assume that any variation in ω for a given arc line should be approximately linear within a given v-groove block of fibers mounted to the pseudo-slit. This is because all fibers in a given block will have a common telecentricity with common alignment errors, and should vary in profile only smoothly with the gradual curvature of the slithead. Figure 3 (left-hand panels) shows that this is the case; while individual measurements for a given fiber are noisy, they describe smooth well-defined trends within a given block with discrete jumps between adjacent blocks corresponding to alignment differences in their mounting on the pseudo-slit. We therefore replace the individual measurements of each arc line in a given fiber with the linear polynomial fit to the fibers in each block; this polynomial fit

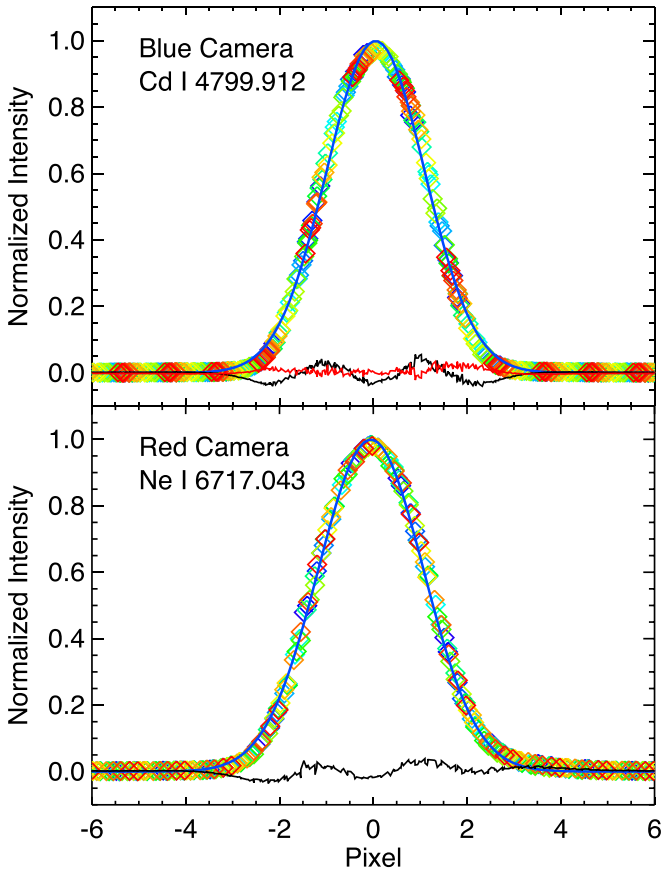

Figure 2. Super-sampled observational arc-line profile for characteristic spectral lines in the blue and red cameras. Colored points represent flat-fielded spectra for $\sim$30 fibers in a single v-groove block for which the LSF is constant across fiberid to <1% but the change in zero-point of the wavelength solution results in the arc line falling at a variety of different pixel phases for different fibers (color-coded by fiber number). The solid blue line in both panels represents a Gaussian model fit to the observed data points similar to that used by the MaNGA DRP to describe the line profile, while the solid black line shows the residual difference between the observational data points and the Gaussian model. These residuals demonstrate that the true line profile is modestly platykurtic due to the circular image of the undispersed optical fiber spot; for comparison, a model line profile composed of a Gaussian convolved with a top-hat response function can reproduce the observations with negligible residuals (top panel, red solid line).

reduces the typical ω uncertainty by a factor of about $\sqrt{30}$ (as there are roughly 30 fibers in each block), corresponding to an improvement from $\sim$1% to $\sim$0.2% in the wavelength range $\lambda\lambda$6500–7000 Å. This replacement also has the added benefit of allowing us to be robust against occasional critical failures of the Gaussian-fitting algorithm (resulting, e.g., from bad pixels or cosmic rays).

Next, we assume that ω within each fiber should vary smoothly as a function of wavelength within the range $\lambda\lambda$3500–6300 Å (blue cameras) and $\lambda\lambda$5900–10300 Å (red cameras). We therefore fit the linearly interpolated ω in each fiber with an nth-order polynomial, where $n = 5/6$ for the blue/red cameras, respectively.[19] As illustrated in Figure 3 (middle panels), these trace-sets can be evaluated throughout the entire MaNGA wavelength range, and they do a good job of reproducing the observed widths at individual arc lines. In the 6000–7000 Å range, the density of arc lines is particularly high,

[17] Although some early commissioning observations showed optical coma at the longest wavelengths in the red camera of spectrograph 1, this was resolved by realignment of the camera optics prior to the start of the majority of the survey.

[18] Typically the instrumental LSF is represented as $\sigma_{\rm instr}$, but to avoid a proliferation of subscripts, we assign the LSF its own variable.

[19] These orders are determined empirically to be the minimum necessary to fit the observed variation.

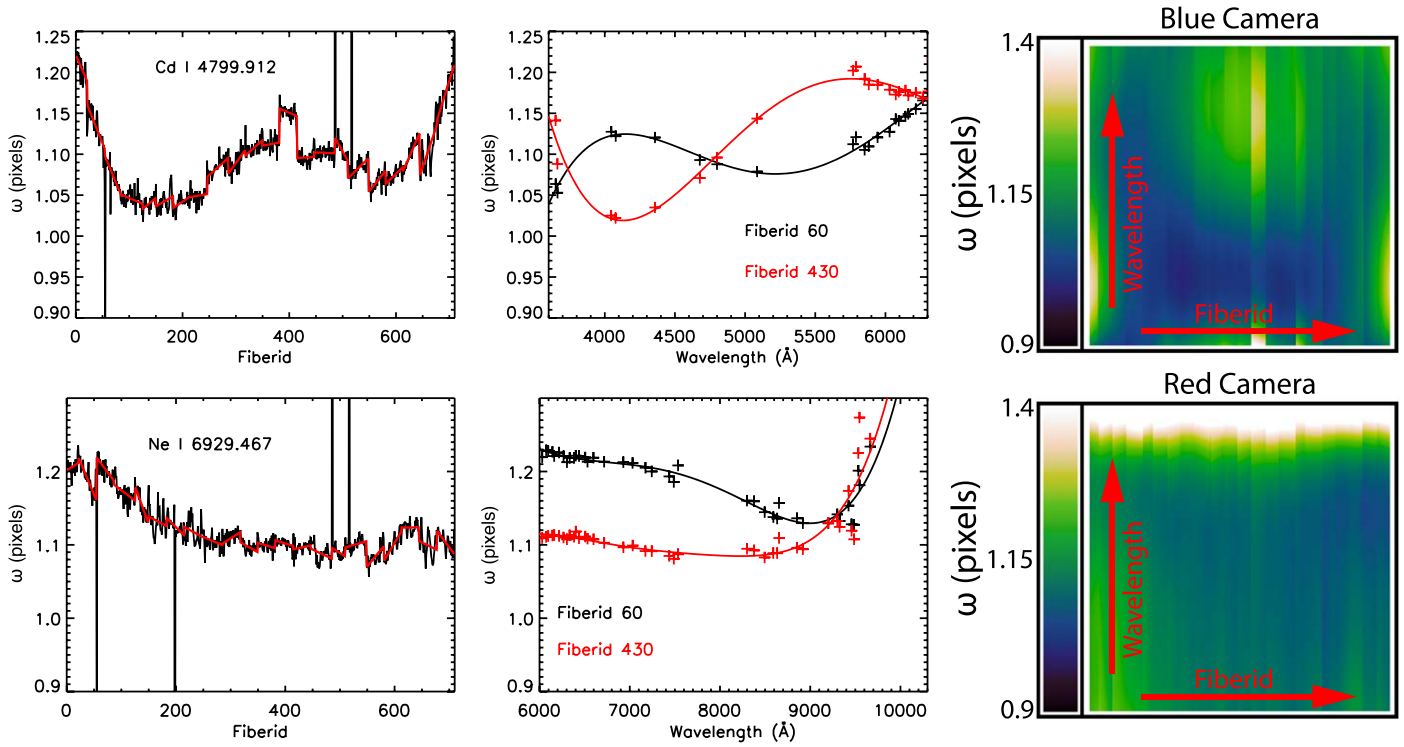

Figure 3. Estimates of the MaNGA LSF (ω) derived from observations of Neon–Mercury–Cadmium calibration lamps. Left-hand panels: measured values of ω (black line) as a function of fiberid for the indicated lamp line in the blue (top row) and red (bottom row) cameras. Extreme outliers are due to failures in the fitting routine caused by cosmic rays, detector artifacts, and similar effects. The solid red line shows the fit assuming linear variation within each v-groove block and allowing for arbitrary jumps between blocks. Middle panels: measured values of ω as a function of wavelength for two example fibers (fiberid 60/430, black/red points, respectively) in each camera. The solid black and red lines represent the polynomial traceset fit to the observations. Right-hand panels: polynomial traceset fits to ω evaluated across all fiberid and wavelengths in the scientifically relevant sections of the detectors (3600–6300 Å and 6000–10300 Å for the blue/red cameras, respectively). All data shown here are taken from exposure 204255, plate 7960, MJD 57280 (spectrograph 1, cartridge 4).

and ω varies particularly slowly with wavelength; the scatter of individual arc lines about the model relation suggests that the overall uncertainty of the fit in the Hα wavelength regime is about 0.5%.

Figure 3 (right panels) illustrates the resulting arc-lamp model for ω across the blue and red cameras; we note that while ω in the red cameras is relatively flat as a function of both fiberid and wavelength (rms ~0.01 pixels below 9000 Å), ω in the blue cameras shows significantly more structure (rms ~0.03–0.04 pixels between 4000 and 6000 Å), corresponding both to the overall curvature of the focal plane and global alignment differences between blocks of fibers. The details of this structure are cartridge-dependent since the slithead on each of the six cartridges has its own mechanical alignment. Generally, however, fibers ~25% and 75% of the way along each slit have up to a factor ~2 lower and more constant ω with wavelength, while fibers near the middle or ends of the slit show larger variations.

3.2. Pixel Broadening

As indicated by Figure 3, MaNGA is nearly critically sampled since spectrally unresolved arc lines typically have a 1σ width of about $\omega = 1.0$–1.2 pixels (2.4–2.8 pixels per FWHM). As discussed extensively by Robertson (2017, see their Figure 16), such pixels are sufficiently large compared to the intrinsic LSF delivered by the telescope/spectrograph optics that the effective LSF is broadened by the convolution with the top-hat response of the detector pixels. Our post-pixellized measurements of ω that were obtained by simply evaluating a Gaussian profile model at the midpoint of each pixel are therefore systematically biased relative to the "true" intrinsic instrumental dispersion before convolution with the pixel response function (i.e., the pre-pixellized ω).

We compute the magnitude of this effect using Monte Carlo simulations in which we constructed 10x over-sampled Gaussian models of known width, convolved them with the pixel response function at a variety of pixel phases, and then measured the resulting profiles using the commonly available Gaussian-fitting techniques that simply evaluate the Gaussian function at the pixel midpoints. As illustrated in Figure 4, post-pixellized widths are systematically broader than the pre-pixellized values by ~1%–10%, and they define an extremely tight mathematical relation in which the pixel-sampling phase drives the scatter but is of negligible importance (<0.1%) in the range of line widths observed by MaNGA. The DRP therefore computes pre-pixellized estimates of the MANGA LSF ($\omega_{\rm PRE}$) from the measured post-pixellized values ($\omega_{\rm POST}$) using a fourth-order polynomial fit to this relation (red line in Figure 4).

As motivated and discussed in Section 4, the MaNGA DAP adopts these pre-pixellized estimates of ω and rigorously accounts for pixel convolution. However, since many third-party analysis routines ignore pixel convolution and instead rely on simple Gaussian-fitting approximation, the DRP provides both $\omega_{\rm POST}$ and $\omega_{\rm PRE}$ with all of the survey data products.

3.3. Skyline Model

In practice, differences in the telescope focus (due to, e.g., changing weather conditions), gravitational flexure of the

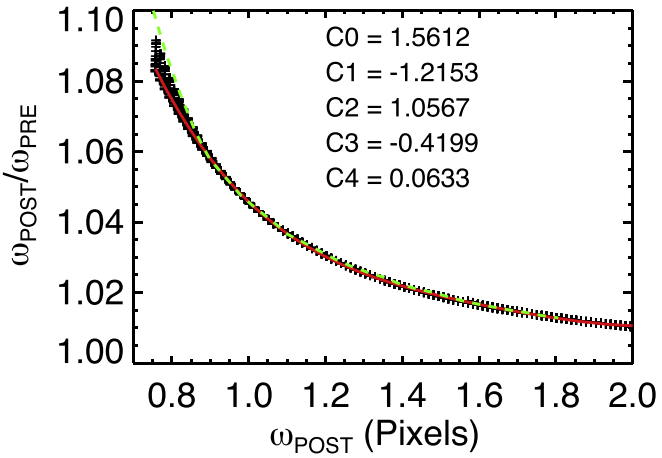

Figure 4. Systematic overestimate of the true spectral LSF (ω_{PRE}) as a function of the LSF derived from fitting a Gaussian profile (ω_{POST}) to a series of Monte-Carlo-generated mock arc-lamp spectra. Each black "+" symbol represents a single test with a different pixel phase; differences between pixel phases are only apparent at the smallest $\omega_{POST} \sim 0.8$ pixels, at which the peak-to-peak scatter is about 1%. In the typical MaNGA range ($\omega_{POST} = 1.02/1.11/1.31$ pixels for the 5th/50th/95th percentiles of the MPL-10 distribution), pixel phase effects are less than 0.1%. The solid red line represents the fourth-order polynomial fit to this relation used by the DRP; the coefficients of this fit are given in the inset text. Also shown for comparison (dashed green line) is the similar relation derived by Robertson (2017).

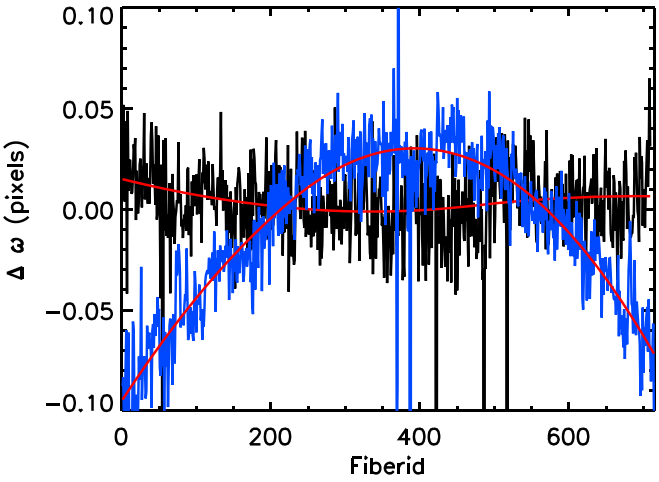

Figure 5. Difference $\Delta\omega$ between the measured O I λ5577.339 skyline LSF and the arc-lamp model evaluated at the skyline wavelength for a typical case (7960-57280-204255-b1; black solid line) and for a large-shift case (7960-57458-216817-b2); blue solid line). In each case, the solid red line shows the cubic spline fit to the observed values used by the MaNGA DRP.

spectrographs, and various other effects mean that the LSFs derived from arc-lamp exposures are only an approximation to the actual LSF of any given science exposure. We therefore use the well-known bright sky emission-line features to refine the LSF estimate for each individual science exposure.[20]

Unlike the arc spectra, however, the night-sky emission features are not ideally distributed in wavelength (there are very few bright skylines at blue wavelengths), and they can frequently be biased by continuum emission and blends of multiple atomic and/or molecular transitions. While such blending may be weak, even weak blending can bias apparent measurements of the LSF at the few-percent level. Rather than re-deriving the LSF solution from the skylines, the DRP therefore uses them to simply make low-order adjustments to the arc-line model.

Using the extracted, flat-fielded science frame spectra, we fit each skyline in our list of reliable lines (see Table 2) with a post-pixellized Gaussian model that includes a linear polynomial term to account for wavelength gradients in the sky continuum level. We then compute the difference $\Delta\omega = \omega_{sky} - \omega_{arc}$, where ω_{arc} is the arc-line LSF model evaluated at the wavelength of the skyline features. Even in the cases for which the sky and arc line measurements differ substantially, the difference $\Delta\omega$ between the measurements shows an extremely smooth variation along the slit with no noticeable block-to-block jumps and only statistical noise from the individual fiber measurements (Figure 5). We therefore fit (unmasked) values of $\Delta\omega$ with a cubic basis spline with breakpoints every 150 fibers to obtain our initial estimate of the difference between skyline and arc line LSF models.

[20] Such refinements are not possible for the shortest MaStar exposures in which even strong skylines are relatively faint, but since these exposures are obtained much closer in time to the calibration exposures, focus drifts are much less common than in longer MaNGA observations, which can differ by an hour from the calibration exposures.

Table 2
Night-sky Calibration Lines

Wavelength (Å)	Transition
4046.56[a]	Hg I
4358.33[a]	Hg I
5460.94[a]	Hg I
5577.339	O I
6300.304[a]	O I
6363.776	O I
7571.75	OH
7794.12	OH
7821.51	OH
8399.16	OH
8430.17	OH
8885.83	OH
8919.61	OH
9439.65	OH
9872.13	OH
10124.01	OH

Note.
[a] Used only for adjustment of the wavelength solution, not adjustment of the LSF.

In the blue camera ($\lambda\lambda = 3600$–6300 Å), only the bright O I λ5577.339 skyline is deemed to be a reliable LSF calibrator since all of the other lines used to adjust the MaNGA wavelength solution are marginally blended at the few-percent level, and the $\Delta\omega$ derived from this line is therefore assumed to be constant for all wavelengths. In the red camera ($\lambda\lambda = 5900$–10300 Å), there are multiple skylines, but since we observe no unambiguous trends in $\Delta\omega$ with wavelength, we simply median combine each of the estimates to obtain our final correction value. The resulting sky-adjusted LSF models are typically different from the original arc-line models by less than 0.01 pixels, although in some extreme cases can differ by around 0.05 pixels (Figure 6, middle and right-hand panels, respectively). Based on the >22,000 individual science exposures in MPL-10, we note that the arc-line model tends to systematically underestimate the observed skyline width by

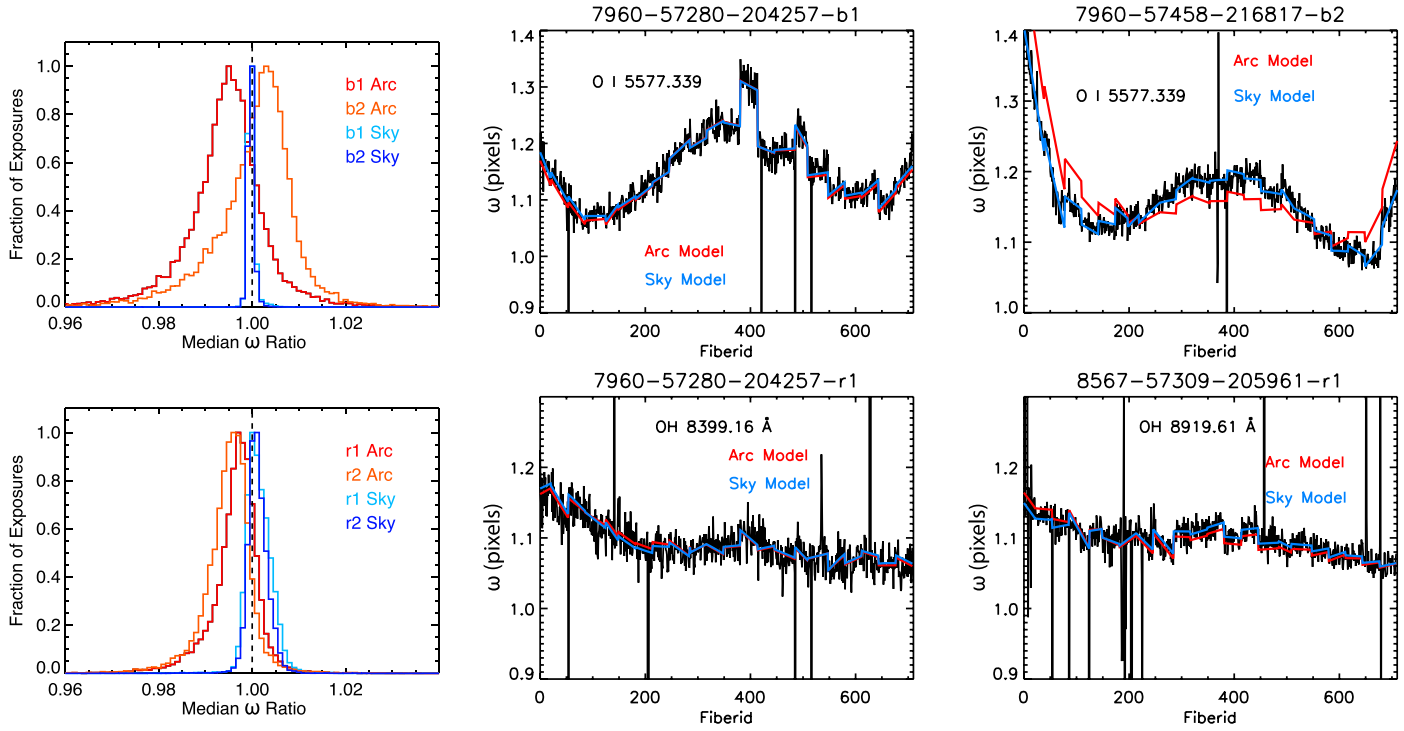

Figure 6. Left column: histogram of the median ratio per exposure between the arc-line and skyline LSF models, and between the skyline LSF models and the individual skyline measurements for the ∼22,000 individual science exposures in MPL-10. While the width of the arc-line histograms is dominated by the differences between the arc model and the skyline measurements, the skyline histogram width is dominated by the uncertainty in the skyline measurements. Note that the blue histograms are narrower than the red as they are based on a single skyline. Middle column: measured skyline widths (black solid line) as a function of fiberid compared to the arc-line and skyline models (solid red and blue lines, respectively) for a typical case in the blue and red cameras. Right column: the same as the middle column, but for a large-shift example. Note that the skyline model does not always go through the middle of the observed skyline measurements for a given line in the red camera, because individual lines can have systematic biases due to blending and continuum-fitting problems.

∼0.5% on average in the b1, r1, and r2 cameras, and overestimates the skyline width by about the same amount in the b2 camera (Figure 6, left-hand panels), possibly due to systematic differences in optical alignment between the cameras. In contrast, the skyline-adjusted models have a negligible systematic offset from the skyline measurements and a significantly smaller width to the distribution that is dominated by the uncertainty in individual lines.

3.4. Wavelength Rectification and Dichroic Recombination

As discussed in detail by Law et al. (2016), the MANGA DRP processes each camera of data independently up to the point of producing flux-calibrated, sky-subtracted spectra for each fiber. Once all four cameras have been thus processed, the DRP stitches together the natively sampled spectra from the blue and red cameras across the dichroic break to produce final calibrated spectra for each fiber that cover the entire MaNGA wavelength range. This is achieved via high-order cubic basis spline modeling of the blue and red spectra with a tapered inverse variance weighting[21] in the 5900–6300 Å dichroic window to provide a smooth transition between the cameras. This spline model is evaluated on two different output grids: a linear solution with a constant $\Delta\lambda = 1$ Å and a logarithmic wavelength solution with a constant $\Delta\log(\lambda/\text{Å}) = 10^{-4}$. While the linear wavelength solution products are used for some MaNGA value added catalogs (e.g., Pipe3D; Sánchez et al. 2016), the MaNGA DAP (Section 4) uses the products with a logarithmic wavelength solution.

The combination of the per-camera LSF vectors onto the final rectified wavelength grid uses the same algorithm as for the spectra themselves. In the 5900–6300 Å dichroic overlap region, the gradual tapering of the weights applied to the blue/red cameras serves to produce a smooth transition between the LSF solutions of the individual cameras, but the spectra are nonetheless a composite of individual spectra whose LSF widths differ from each other by about 15%. As we show in Figure 7 however, the non-Gaussianity introduced as a result is insignificant, especially compared to the known intrinsic line profile (Figure 2).

In addition to simply mapping the LSF onto the output wavelength grid however, the wavelength rectification also broadens the effective LSF slightly compared to the original spectra that were sampled by the native detector pixels. We compute the magnitude of this broadening using a series of Monte Carlo simulations for a statistically large grid of Gaussian "comb" spectra, in which artificial spectra with emission lines of known width are created every 100 Å throughout the MaNGA wavelength range. These artificial spectra are produced using the wavelength solution of a typical natively sampled exposure and then combined together across the dichroic to produce composite spectra using the spline algorithm described above. The widths of the resulting lines are then computed via Gauss-fitting techniques to compare to the known input widths. By repeating this experiment across the 700+ fibers per MaNGA spectrograph, shifting the input line centroids by sub-pixel values to consider ten different input pixel phases, and covering a range of

[21] Smoothed to mitigate the well-known systematic biases that inverse variance weighting can introduce in the median counts of combined spectra.

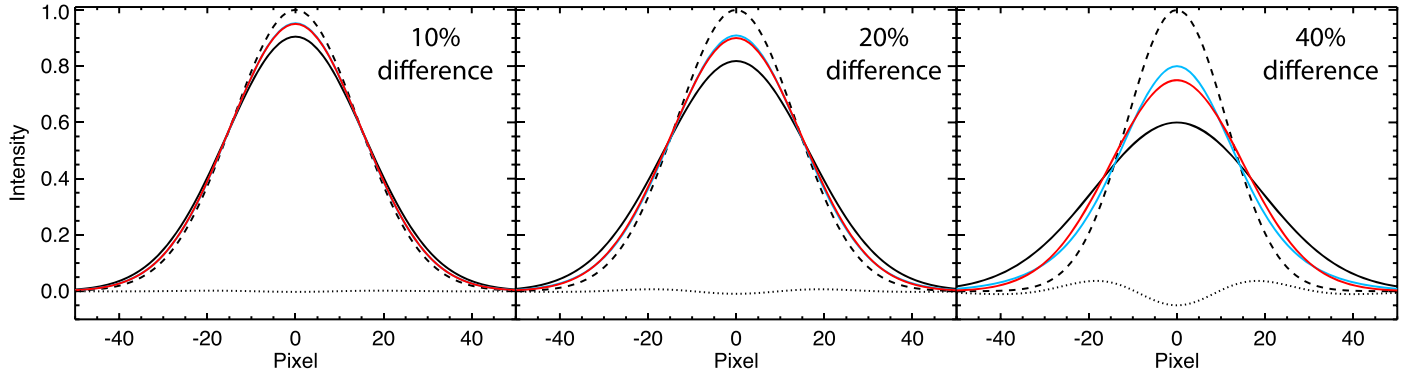

Figure 7. Comparison between Gaussian LSF models produced by summing Gaussians of various widths. In each panel, the solid and dashed black lines, respectively, show Gaussian profiles whose widths differ by the indicated amount at fixed integrated line intensity. The blue line indicates the profile produced by summing the solid/dashed black profiles, while the red line indicates the profile of a single Gaussian whose width is given by the average of the first two. The dotted black line shows the residual difference between the true summed profile (blue line) and the approximate Gaussian model profile (red line). These residuals are small compared to the known non-Gaussianity of the instrumental profile (Figure 2) for the typical difference in LSF widths ($\lesssim$15%) combined by the MaNGA DRP.

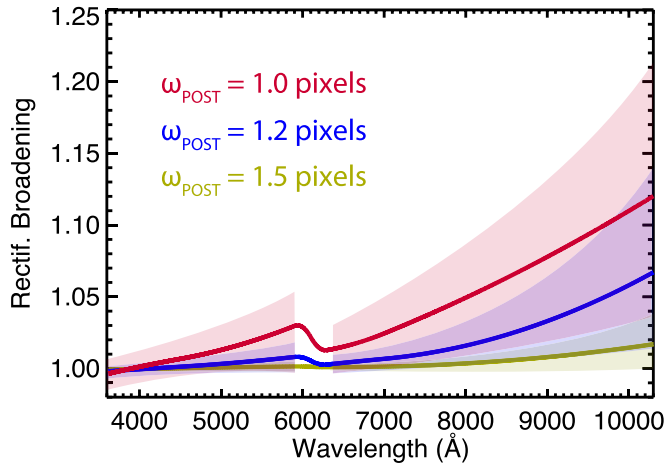

Figure 8. Effective LSF broadening factor (i.e., the ratio of the post-pixellized LSF in units of angstroms measured before and after rectification) introduced by the spectral rectification of the native-pixel blue and red camera spectra onto a fixed logarithmic wavelength grid. Solid red, blue, and gold lines show the median broadening as a function of wavelength computed via Monte Carlo analysis of artificial spectra for input widths of $\omega = 1.0$, 1.2, and 1.5 pixels, respectively. In each case, the shaded region shows the 1σ variation about the mean traced by input lines with different effective pixel phases. The corresponding curves for the linear wavelength grid (not shown) are generally similar except in the 9000–10000 Å range where the logarithmic output grid under-samples the typical input LSF.

12 different input widths from 0.9 to 2.0 pixels, we are therefore working with a grid of >6 million simulated lines.

As shown in Figure 8, the effective broadening factor (post-pixel to post-pixel) is a strong function of wavelength, increasing from near unity at the shortest wavelengths in both the blue and red cameras to a ∼10% effect at the longest wavelengths in the red camera for input $\omega_{\rm POST} = 1.0$ pixels. The exact correction factor is strongly dependent on the input pixel phase, particularly for values of $\omega_{\rm POST} \leqslant 1.0$ pixel. Since any DRP correction to the LSF cannot take pixel phase into account (since this will be different for every emission line in the science data in a manner that cannot easily be modeled), we fit the median relation as a function of wavelength[22] for each of our 12 input widths with a cubic basis spline to compute a grid of correction factors for both the logarithmic and linear wavelength solutions. The DRP then corrects the composite LSF vectors for each fiber by the appropriate value interpolated from this reference grid (applying the same factor to both $\omega_{\rm PRE}$ and $\omega_{\rm POST}$ estimates). Given the typical range of $\omega_{\rm POST} =$ 1.1–1.2 pixels in the vicinity of Hα, the range of correction factors across different pixel phases indicated by Figure 8 suggests that the rms uncertainty of the applied correction is typically around 1%.

[22] We do not include the dichroic overlap region in our fit since different LSF widths from the blue and red cameras are being combined here into a single line profile, but instead simply ensure that the spline model smoothly joins between the blue and red camera solutions.

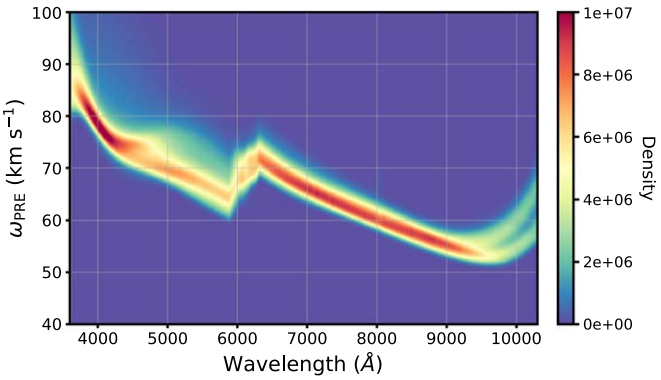

Figure 9. Density plot of the pre-pixellized instrumental LSF (in velocity units) reported by the MaNGA DRP for all ∼31 million individual fiber spectra in MPL-10 (for the LOG wavelength solution).

The corrected pre-pixel instrumental LSFs for all individual calibrated exposures (∼30 million individual fiber spectra) in MPL-10 are shown in Figure 9. We conclude that the typical instrumental resolution improves from 80 to 90 km s^{-1} at the bluest wavelengths to about 55 km s^{-1} at the red end of the MaNGA wavelength range, with the largest rms variation between fibers around 5000–6000 Å and the smallest rms variation of just a few percent around Hα.

3.5. Data Cube Construction

The DRP additionally reformats the calibrated fiber spectra into a rectilinear data cube in which the individual fiber spectra have been coadded to produce a single 3D data cube with two spatial axes and one spectral axis. Working with these data cubes is significantly easier than working directly with the individual calibrated fiber spectra (provided by the DRP as

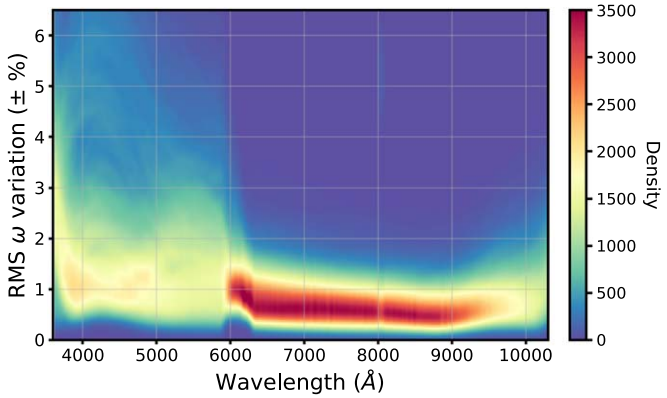

Figure 10. rms variation of $\omega_{\rm PRE}$ as a function of wavelength between all fiber spectra contributing to a given data cube for all 10,523 data cubes in MPL-10.

"row-stacked spectra," or RSS) as the latter suffer from chromatic differential refraction while the spectra in the rectified data cubes are directly associated with a specific location on the sky. For this reason, the vast majority of the MaNGA science team has thus used the composite data cubes for science analyses, as does the MaNGA DAP.

However, the algorithm used to construct these data cubes produces complications of its own. In addition to introducing strong spatial covariance between adjacent data cube spaxels, as explored in detail by Law et al. (2016, Section 9) and Westfall et al. (2019, Section 6), the data cube construction also combines spectra with a variety of different spectral resolutions. Since the effective LSF can vary strongly from fiber to fiber, exposure to exposure, and night to night, the range of input resolutions contributing to any given data cube spaxel can be non-negligible.

Figure 10 shows a density plot of the rms variation in ω of all fibers contributing to a given data cube as a function of wavelength for all 10,523 data cubes in MPL-10. As discussed in Law et al. (2016), typical IFUs show variability at the 1%–2% level in the blue cameras with rare worst-case outliers at about 10%–15% at some wavelengths for IFUs on the edges of the slit. In contrast, driven by the flatter focal plane across the CCDs, the focus in the red cameras is significantly flatter than in the blue, with the majority of all data cubes showing $<1\%$ variability in the component fiber spectra. Given this relatively small LSF variability, we avoid the complexity of attempting to convolve all fiber spectra to the same resolution (i.e., the difficulty in making such small adjustments to the *wavelength-dependent* resolution, the loss of information by degrading the majority of the data cube spectra, and the introduction of more spectral covariance; see, e.g., Pace et al. 2019) and instead construct an LSF width metric for the combined spectra. In other words, assuming a Gaussian function for the astrophysical line-of-sight velocity distribution (LOSVD), we want a simple metric that can be used to accurately remove the influence of the LSF on our measurement of the astrophysical velocity dispersion.

To understand the influence of the LSF metric, we perform an experiment by constructing two Gaussian profiles, each with a width defined by perturbing ω by a small percentage above and below 70 km s^{-1} (e.g., we denote a 1% change as $\delta\omega/\omega = 0.01$). We then construct an "observed" profile by summing these two Gaussian profiles and convolving the result with a third Gaussian with dispersion $\sigma_{\rm in}$ that represents the LOSVD of the gas in the galaxy. We then fit a fourth

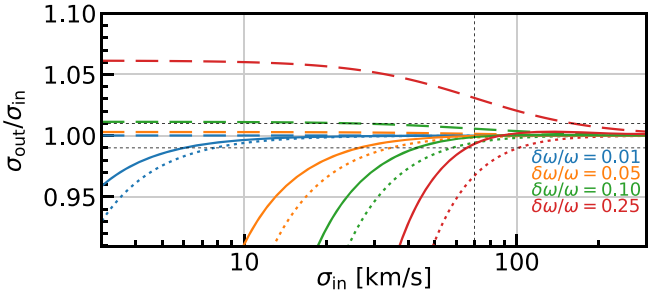

Figure 11. Numerical tests of the bias in the recovered astrophysical velocity dispersion ($\sigma_{\rm out}$) compared to a known input value ($\sigma_{\rm in}$) for three different descriptions of a composite LSF width. Line types indicate the method used to construct the composite LSF width (see the text) while line color indicates the variation in the LSFs combined to construct the composite LSF ($\delta\omega/\omega$; see legend). From Figure 10, we know that the MaNGA LSF variation is typically $\lesssim$1%–2% (blue lines), such that the exact definition of the composite LSF width is effectively irrelevant for $\sigma_{\rm in} > 10$ km s^{-1}.

Gaussian to the result, mimicking the typical procedure when fitting galaxy data. The dispersion of the best-fitting Gaussian is then corrected for the LSF width to produce $\sigma_{\rm out}$; any difference between $\sigma_{\rm in}$ and $\sigma_{\rm out}$ indicates a measurement bias. The experiment is performed with highly over-sampled noiseless profiles so as to explore the *intrinsic* bias in each approach.

In Figure 11, we show the results of this test for four values of $\delta\omega/\omega$ (differentiated by line color) and three different methods of estimating the combined LSF metric: (1; dotted lines) the second moment of the summed profile $\omega^2 = (\omega_{\rm lo}^2 + \omega_{\rm hi}^2)/2$, where $\omega_{\rm lo}^2$ and $\omega_{\rm hi}^2$ are the values for the narrow and broad Gaussian components, (2; solid lines) the mean ω of the two components, and (3; dashed lines) the width of a new Gaussian profile fit directly to the summed profile.

Figure 11 demonstrates that when the range in LSF widths for combined spectra is $\lesssim$1% (true for the majority of MaNGA data cubes, particularly for $\lambda \gtrsim 6000$ Å), the method used to estimate the combined LSF is largely irrelevant; any bias is $<1\%$ for $\sigma_{\rm in} > 10$ km s^{-1} for all methods. For larger differences in the LSF widths, fitting the composite LSF to define ω is generally better than the other two definitions. However, given that this method requires significantly more computational overhead—requiring us to construct the composite profile and fit a Gaussian for every pixel with valid spectral data in the full MaNGA data set—and the fact that it indeed introduces biases of its own, we instead adopt the simple mean method, which performs modestly better than using the second moment. Combined with Figure 10, we expect that this simple mean method of combining the fiber LSFs will rarely introduce more than a 1 km s^{-1} bias for $\sigma \gtrsim 20$ km s^{-1} even in the extreme case of 5% variation in the fiber ω, and will more typically be <0.1 km s^{-1} (far below the typical uncertainty in the individual measurements; see Figure 15). As illustrated by Figure 7, differences in the LSF of the input spectra at such levels will have a negligible impact on the overall Gaussianity of the composite spectrum.

We therefore construct LSF data cubes using the same algorithm and weighting scheme as adopted to construct the science data cube. That is, with the modified Shepard algorithm, the image of the galaxy at a given wavelength slice is a weighted sum of the input fiber spectra at that wavelength, and the LSF "image" is constructed from the same weights applied to the LSF vectors of the individual fibers.

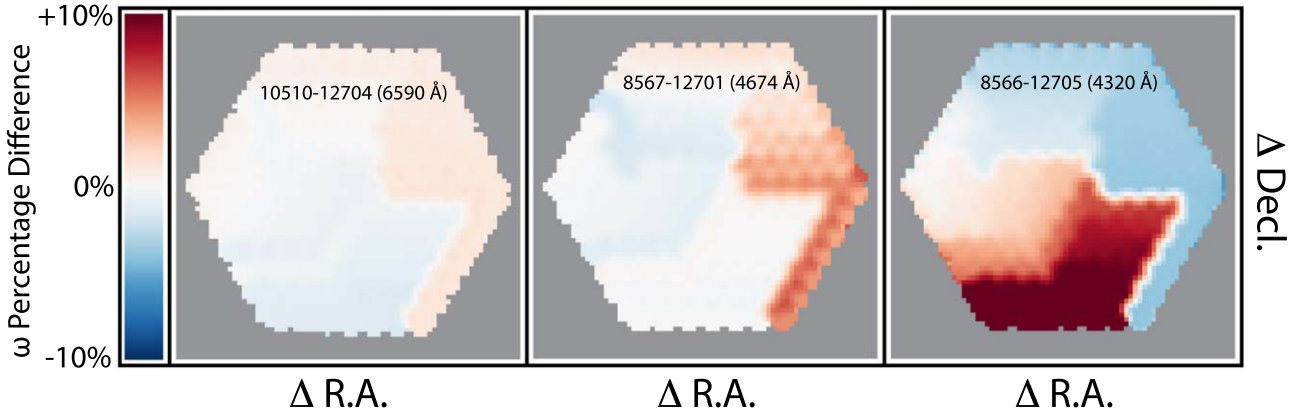

Figure 12. Spatial variability in ω for three example data cubes at various wavelengths (left to right: 1%, 2%, and 6% rms variability). The visible structure traces the mapping of the IFU fibers to discrete V-groove blocks on the BOSS spectrograph pseudo-slit (see Figure 9 of Drory et al. 2015, with a horizontal flip in orientation). Inset text gives the MANGAID and wavelength of each example.

The MaNGA DRP provides both a summary averaged LSF vector for each data cube (as small variations will be unimportant to science cases studying astrophysical line widths in excess of 100 km s^{-1}), as well as a full 3D LSF data cube so that downstream analysis programs can use the effective LSF appropriate for each spaxel in the cube. For illustrative purposes, we show in Figure 12 examples with 1%, 2%, and 6% LSF variation across the face of the IFU as calculated by the DRP. Such spatial variation in the effective LSF of integral-field data is well known for slit-type and lenslet-type spectrographs as well (see, e.g., Figure 6 of Law et al. 2018) and must be taken into account when measuring velocity dispersions near the instrumental resolution or below. As suggested by Figure 10, 99.9% of cubes resemble the 1% or 2% rms examples at red wavelengths, while 80% resemble these examples at blue wavelengths.

3.6. LSF Differences from Prior Data Releases

As the MaNGA DRP has evolved over the survey, the estimated instrumental LSF too has changed. Rather than representing significant changes in the data, as outlined in the previous sections, this instead reflects our evolving understanding of the instrument and improvements to our methods of characterizing the data. These changes are summarized in Figure 13, which plots the ratio between ω for all MPL-10 fiber spectra that were included in four of the major internal/external MaNGA data releases and shows that the MaNGA LSF estimates have generally been converging over the lifetime of the survey.

Relative to MPL-10, MaNGA's initial public data release (DR13, released Summer 2016) systematically overestimated the pre-pixellized LSF in the far blue by 10%–15% while underestimating it in the red by 5%–10%. This changed with the release of DR14 (Summer 2017), which made an initial correction to broaden the pre-pixellized LSF measurements to post-pixellized values during the skyline adjustment stage, in addition to including a term to account for the broadening factor contributed by the wavelength rectification of fiber spectra (see Abolfathi et al. 2018). These changes generally improved performance at red wavelengths but were an overcorrection, leading to a ∼5% effective overestimate of the LSF around Hα.

DR15 (Summer 2018) for the first time provided simultaneous measurements of the pre-pixellized and post-pixellized LSF in full cube format, fixed the LSF overestimate in the far blue (by rejecting the partially blended Cd I $\lambda\lambda$3610 and low-quality Hg II $\lambda\lambda$3984 arc-lamp lines and substituting Hg I $\lambda\lambda$3663 instead), and implemented a Gaussian-comb solution for measuring the broadening due to wavelength rectification (instead of relying upon measurements of individual lines). As illustrated by Figure 13, the combination of these changes brought all wavelengths relatively well in line with MPL-10, but with a ∼4% underestimate of the LSF around Hα. Minor additional changes to polynomial fitting orders and rejection of additional skylines implemented in MPL-9 in turn decreased this difference to around 2%–3%.

Relative to MPL-9, MPL-10 completely overhauled many aspects of the LSF estimation. Most fundamentally, instead of using legacy C code dating back to the original SDSS spectro survey to measure the pre-pixellized LSF (and later bootstrap the corresponding post-pixellized LSF), it instead uses new code to measure the post-pixellized LSF and later bootstraps the pre-pixellized values based on extensive Monte Carlo simulations (Section 3.2). Additionally, MPL-10 introduced further modifications to the reference arc and skyline lists and polynomial fitting orders.

The scientific impact of this evolution in the estimated LSF will depend on the range of astrophysical velocity dispersions considered by a given analysis. Above $\sigma_{\mathrm{H}\alpha} = 100$ km s^{-1}, the systematic error in recovered velocity dispersions after correcting for the instrumental resolution will be less than 3%. At velocity dispersions far below the instrumental resolution though, the changes in the estimated LSF become increasingly important, and around $\sigma_{\mathrm{H}\alpha} = 30$ km s^{-1}, analyses using DR13, DR14, or DR15 data will have derived values that are systematically too high by ∼30%, too low by ∼30%, and too high by ∼20%, respectively compared to MPL-10.

4. Spectral LSF in the MaNGA DAP

The MaNGA DAP is the survey-led software package that derives astrophysical measurements from the DRP data cubes. These measurements are produced by five core modules with the following primary purposes: (1) spatially bin the data to meet a g-band continuum signal-to-noise ratio (S/N) using the Voronoi binning method of Cappellari & Copin (2003); (2) measure stellar kinematics by performing full-spectrum fitting using pPXF (Cappellari & Emsellem 2004; Cappellari 2017) with the emission lines masked; (3) calculate moments of the emission-line profiles to obtain nonparametric (pixel-summed)

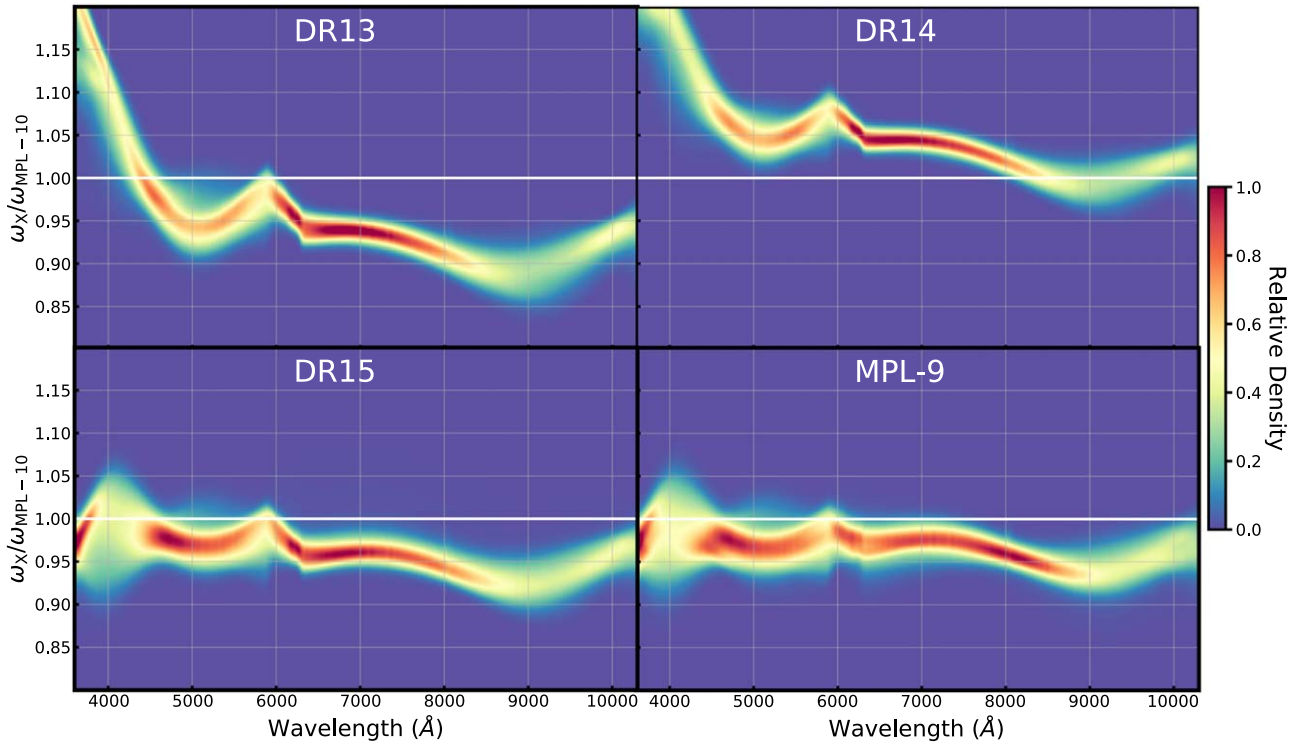

Figure 13. Evolution of the MaNGA LSF estimate over the lifetime of the survey. Each panel shows a density plot of the ratio between the LSF vectors for all fiber spectra in common between MPL-10 and prior data releases DR13, DR14, DR15, and MPL-9.

fluxes and equivalent widths; (4) fit single-component Gaussian profiles to the emission lines with simultaneous readjustment of the stellar continuum using pPXF; and (5) measure spectral indices, including both absorption-line indices (e.g., $H\delta_A$; Worthey & Ottaviani 1997) and "break" indices (e.g., D4000; Bruzual 1983). Detailed descriptions of these modules and tests of the efficacy and performance of the DAP are provided by Westfall et al. (2019) and Belfiore et al. (2019), with the latter focusing specifically on the emission-line modeling. Below, we discuss the full-spectrum-fitting modules of the DAP (i.e., modules 2 and 4 above) and their corresponding treatment of the spectral LSF.

4.1. Overview of Spectral Fitting in the DAP

The pPXF approach operates on the fundamental assumption that a galaxy spectrum is composed of a linear combination of template spectra convolved with a template-dependent LOSVD. Ignoring any multiplicative (e.g., attenuation, flux-calibration) or additive (e.g., sky-subtraction) effects and explicitly including the convolution by the pre-pixel spectral-resolution kernel, $\mathcal{R}(\lambda)$, and the pixel-sampling kernel, $\mathcal{S}(\lambda)$, we can write the underlying pPXF assertion as (see Cappellari 2017, Equation (11)):

$$G_j \equiv G' * \mathcal{R}_j * \mathcal{S} \approx \sum_i w_i (T_i' * \mathcal{L}_i' * \mathcal{R}_j * \mathcal{S}), \qquad (1)$$

where $*$ denotes a wavelength-dependent convolution, $\mathcal{L}_i'$ is the *intrinsic* LOSVD kernel, G' and T_i' are the *intrinsic* spectra of the galaxy and template object, respectively, and the summation runs over each of the individual template objects. We have additionally subscripted the observed galaxy spectrum, G, and the associated spectral-resolution kernel with the index j to emphasize that MaNGA observations have a range in spectral resolution that vary both between observations and between spaxels in a given data cube (Figure 12). Except for templates based on theoretical models, the T_i' are not generally known; instead we have observed spectra that are taken with their own spectral-resolution and sampling kernels; i.e., $T_i \equiv T_i' * \mathcal{R}_i * \mathcal{S}_i$. Solving for T_i', Equation (1) becomes

$$G_j \approx \sum_i w_i \{T_i * \mathcal{L}_i' * (\mathcal{R}_j \overline{*} \mathcal{R}_i) * (\mathcal{S} \overline{*} \mathcal{S}_i)\}, \qquad (2)$$

where we use $\overline{*}$ to signify a wavelength-dependent *deconvolution*. Although pPXF allows for template spectra with a pixel sampling that is a fixed integer factor smaller than the sampling of the galaxy spectrum,[23] any differences in the (pre-pixelized) spectral resolution of the templates and the galaxy data are ignored.

Standard practice is to use templates that have been convolved to exactly the same spectral resolution as the galaxy data, either by observing templates with the same instrument setup or by degrading the spectral resolution of a set of templates to match the resolution of the galaxy data. As we note in Westfall et al. (2019), however, this is hard to do in practice for many reasons: the reproducibility of the instrument setup, the uncertainty in the determination of the wavelength-dependent LSF for both the galaxy and template spectra, and the redshift difference between the galaxy and template objects. Moreover, an analysis of the relevant error propagation implies that it is almost always better to use templates with higher spectral resolution than the galaxy spectra (Westfall et al. 2019,

[23] In this case, the convolution by $(\mathcal{S} \overline{*} \mathcal{S}_i)$ is accomplished via a simple integer rebinning of the convolved template spectra. This functionality ensures that the LSF of the template spectra is still well sampled, even when the templates have substantially higher spectral resolution compared to the galaxy spectrum.

Appendix B). In the MaNGA DAP, we therefore chose to use pPXF to fit the galaxy data using templates at their native spectral resolution. This means that we must construct a correction that accurately removes the effect of the template-galaxy spectral-resolution difference to recover the parameters of the astrophysical LOSVD. In terms of Equation (2), our approach is to have pPXF fit $\mathcal{L}_{ij} = \mathcal{L}'_i * (\mathcal{R}_j \overline{*} \mathcal{R}_i)$—the kernel composed of the astrophysical LOSVD convolved with the template-galaxy instrumental resolution difference—and then we construct a correction to $\mathcal{L}_{ij}$ that yields $\mathcal{L}'_i$. The details of how the DAP constructs the corrections are different for the ionized gas and the stars; however, both currently assume that the template LSF, the MaNGA LSF, and the LOSVD are single-component Gaussian profiles. This means that the only parameter of $\mathcal{L}_{ij}$ that requires correction is the velocity dispersion.

The key difference between the velocity-dispersion corrections derived for the stars and ionized gas is that the former ignores the wavelength dependence of $(\mathcal{R}_j \overline{*} \mathcal{R}_i)$, whereas the latter is effectively treated on a line-by-line, wavelength-dependent basis.

The construction of the emission-line templates is described in detail by Westfall et al. (2019, Section 9.1). Taking advantage of the analytic Fourier transform of a Gaussian line profile (Cappellari 2017), we set the spectral resolution of the emission-line templates to match the resolution of the MaNGA data cube up to a quadrature offset in $\omega_{\rm PRE}$, to first order. This is only done once per data cube, meaning that there are second-order differences between the resolution of the emission-line templates and the data given the spaxel-to-spaxel variations in the LSF and the spectral variation in the LSF over the velocity scale of the galaxy's internal motions. That is, $(\mathcal{R}_j \overline{*} \mathcal{R}_i)$ is nearly constant for the emission-line templates. Regardless, the DAP fits the velocity dispersion of each line (except for the line doublets listed in Section 4.2.2) independently, which allows pPXF to account for the second-order LSF effects during the fit. Moreover, by adding the template-line velocity dispersion to the pPXF measurement in quadrature, the measurement reported by the DAP for each emission line is exactly the pre-pixelized velocity dispersion of the *observed* line profile ($\mathcal{L}'_i * \mathcal{R}_j$ from Equation (1)).[24] The corrections needed (and provided by the DAP) to calculate the velocity dispersion of $\mathcal{L}'_i$ consist of, therefore, the *pre-pixelized* width, $\omega_{\rm PRE}$, of the instrumental line profile ($\mathcal{R}_j$ from Equation (1)) at exactly the best-fitting centroid of the line. Specifically, the corrected velocity dispersion of, e.g., the Hα line is:

$$\sigma_{\rm H\alpha} = \sqrt{\sigma^2_{\rm H\alpha,obs} - \omega^2_{\rm PRE}}, \quad (3)$$

where $\sigma_{\rm H\alpha,obs}$ is the pre-pixelized velocity dispersion of the observed line.

In DR15 and subsequent MPLs, the templates used to measure stellar kinematics are based on a set of 42 composite spectra generated by the hierarchical clustering of the 985 empirical stellar spectral of the MILES library (Falcón-Barroso et al. 2011; Sánchez-Blázquez et al. 2006), i.e., the "MILES-HC" library (Westfall et al. 2019, Section 5). The MaNGA spectra are fit only over the MILES spectral range (3575 Å $< \lambda_{\rm rest} <$ 7400 Å). We adopt a wavelength-independent instrumental resolution of $\Delta\lambda = 2.5$ Å for the MILES library (Falcón-Barroso et al. 2011, see, by way of comparison, Beifiori et al. 2011).[25] Given the MaNGA resolution from Figure 9, $(\mathcal{R}_j \overline{*} \mathcal{R}_i)$—and therefore $\mathcal{L}_{ij}$— is wavelength dependent; however, we use pPXF to instead fit a wavelength-independent parameterization of $\mathcal{L}_{ij}$. Given the complications involved in allowing for a wavelength-dependent $\mathcal{L}_{ij}$ and the fact that the stellar kinematics are determined by *all* of the absorption features in the MaNGA spectra, we adopt a simple correction for the stellar velocity dispersion derived from the average difference in the pre-pixelized MaNGA and MILES resolution over the fitted spectral range. The corrected velocity dispersion of the stars is therefore:

$$\sigma_* = \sqrt{\sigma^2_{*,\rm obs} - \langle \omega^2_{\rm PRE} - \omega^2_{\rm MILES} \rangle_\lambda}, \quad (4)$$

where $\sigma_{*,\rm obs}$ is the velocity dispersion of $\mathcal{L}_{ij}$, $\omega_{\rm MILES}$ is the pre-pixelized instrumental dispersion of the MILES spectra, and the average quadrature difference in the instrumental dispersion ($\langle \omega^2_{\rm PRE} - \omega^2_{\rm MILES} \rangle_\lambda$) is computed over the fitted wavelength range. This approach is shown to be sufficiently accurate for our purposes (Figure 17 from Westfall et al. 2019, see also Section 6.2).

4.2. Updates to the DAP since DR15

Since DR15 we have made a few key improvements to the DAP compared to the algorithms described by Westfall et al. (2019) and Belfiore et al. (2019). Here we update this information briefly before discussing the reliability of the velocity-dispersion measurements in Section 4.3.

4.2.1. Updated Stellar-continuum Templates during Emission-line Modeling

Measurements of the stellar and emission-line kinematics are performed by separate modules in the DAP (i.e., modules 2 and 4, respectively). The stellar kinematics are measured first, with the expected locations of any emission lines masked such that only stellar templates are included in the pPXF fit. For the emission-line kinematics, the stellar and emission-line templates are combined for the pPXF fit with the stellar kinematics fixed to the results obtained by the previous module. An advantage of performing the measurements in separate modules is to, e.g., ensure that the stellar kinematics are uncorrelated with and insensitive to the modeling of the gas components. Although the stellar kinematics are held fixed during the emission-line modeling, the relative weights of the stellar-continuum templates are re-optimized jointly with the emission-line templates to ensure the emission-line properties are not biased by the previous fit (see Belfiore et al. 2019, Section 5.2). This is particularly important when the DAP is used in its "hybrid binning" mode, where the spatial bins used to determine the stellar kinematics (g-band S/N $\gtrsim$ 10) are

[24] Tests have shown that this approach provides results that are virtually identical to a direct fit of a pixelized Gaussian profile to each line profile.

[25] We assume that this is the pre-pixelized LSF width, consistent with our results in Section 6.2. We note the subtle difference between the value used by the DAP from Falcón-Barroso et al. (2011) and the value of $\Delta\lambda = 2.54$ Å quoted by Beifiori et al. (2011). The difference between these two measurements amounts to a 1.6% difference in the MILES instrumental FWHM, which leads to a ~3% difference in σ_* around 50 km s^{-1}. However, note that this uncertainty in the MILES spectral resolution has no effect on the ionized-gas velocity dispersions.

Table 3
Tied Emission Lines[a]

Doublet/pair	Flux ratio
[O II] λλ3726,3729	…
[Ne III] λλ3869,3967	1/0.3
He I λ3889, Hζ	…
[O III] λλ4959,5007	0.35
[N I] λλ5198,5200	…
[O I] λλ6300,6364	1/0.32
[N II] λλ6548,6583	0.34
[S III] λλ9069,9531	0.41

Note.
[a] All pairs listed have their velocity dispersions tied. Only those lines with data in the second column have their fluxes tied.

deconstructed, and the emission-line parameters are fit per spaxel (Westfall et al. 2019, Section 9.2).

In DR15, both full-spectrum fitting modules used the MILES-HC templates to model the stellar continuum. However, given that the templates are re-optimized, this is not strictly required (see, e.g., discussion by Belfiore et al. 2019, Section 4). Therefore, for MPL-9 and later, we switch from the MILES-HC templates in the stellar-kinematics module to a set of templates derived from our own stellar template library (MaStar; Yan et al. 2019) in the emission-line module. This template switch allows us to continue to leverage the higher resolution of the MILES-HC spectra for the stellar kinematics, while taking advantage of the longer spectral range of the MaStar spectra to allow fits to lines such as [S III]λλ9071,9533 lines. Although the details are still being explored, we expect the use of the MaStar spectra to be subject to systematic uncertainties that are of the same order as those found by Belfiore et al. (2019, Section 4).

4.2.2. Updated Line List and Tied Parameters

Since DR15 we have fit additional emission lines to the MaNGA data beyond those listed by Westfall et al. (2019, Table 3) and Belfiore et al. (2019, Table 1), in part to take advantage of the spectral range of the MaStar templates.

These additional lines include the Balmer lines H12 λ3750 and H11 λ3771, He I λ3889, [N I]λλ5198,5200, He I λ7065, [Ar III]λλ7136,7751, Pa-η λ9015, Pa-ζ λ9229, and [S III] λλ9069,9531. We have also changed the adopted fixed flux ratios of some doublets based on an improved calculation (see Table 3).

While the MaNGA DAP treats the stellar component as a single kinematic component (see Tabor et al. 2019; Shetty et al. 2020), each emission line is allowed to be largely independent with a few exceptions. First, the redshift is forced to be the same for all emission lines in a given spaxel by tying all of the velocities together, which helps stabilize the fit (particularly for lines with relatively low flux) against results biased by noise. Second, virtually all of the 35 velocity dispersions are left free, allowing us to mitigate systematic errors due to the second-order wavelength dependence of $(\mathcal{R}_j \overline{*} \mathcal{R}_i)$ for the emission-line templates. The only exceptions to this are the eight line doublets listed in Table 3; note that He I λ3888.6 and Hζ λ3889.1 are tied as a practical matter, given that they are unresolved by MaNGA.

4.3. Precision and Accuracy of the Velocity-dispersion Measurements

Using a combination of idealized recovery simulations and analysis of repeat observations (i.e., galaxies observed on more than one plate and processed into independent data cubes), in Westfall et al. (2019, Section 7.5) and Belfiore et al. (2019, Section 3) we explored the precision and accuracy of the observed line width measurements σ_0 for the stars and emission lines, respectively. Specifically, we found that the formal uncertainties ε_0 reported by the DAP[26] were generally reliable based on comparison with repeated observations, albeit somewhat underestimated at $S/N > 100$ due to small uncertainties in the astrometric registration of individual MaNGA exposures (see discussion by Belfiore et al. 2019).

However, neither Westfall et al. (2019) nor Belfiore et al. (2019) explored the propagation of these uncertainties in the observed line widths (along with uncertainties in the estimated spectral LSF) to the effective uncertainties in the underlying astrophysical LOSVD. Here, we explore the influence of the LSF measurements on the accuracy of the emission-line and absorption-line velocity dispersions, and specifically target the accuracy of astrophysical measurements of the LOSVD $\sigma_{H\alpha}$ (Equation (3)) and σ_* (Equation (4)). The uncertainty ε_{rec} of these astrophysical widths will be a strong function of both the total S/N and the astrophysical width itself (as measurements will become less reliable far below the instrumental resolution).

In Figure 14, we plot the error in the observed velocity dispersion as a function of the S/N for both the Hα line and the stellar continuum. For the Hα line, there is a very tight correlation between the fractional error and the S/N—i.e., $\varepsilon_0 \propto \sigma_0(S/N)^{-1}$—as expected when fitting a Gaussian line profile. The distribution for σ_* is more complicated because ε_0 becomes increasingly independent of σ_0 as σ_0 becomes small relative to the instrumental resolution; this effect is illustrated by analysis of both idealized simulations and repeat observations by Westfall et al. (2019, Figures 19 and 20).

We use the tight relationship between the fractional error in ε_0/σ_0 and S/N for the emission lines to explore the precision and accuracy of the astrophysical measurements of $\sigma_{H\alpha}$ using a series of Monte Carlo simulations. The input for each simulation is the astrophysical LOSVD $\sigma_{H\alpha}$ (for which we adopt a grid from 1 to 100 km s^{-1} stepped every 1 km s^{-1}), the emission-line S/N (for which we adopt a range from S/N = 5–100), the instrumental LSF ω_{PRE} (which, for simplicity, we fix to be 67.6 km s^{-1}, the median at the wavelength of Hα for the MPL-10 sample), the fractional error in the observed line width ε_0/σ_0 at a given S/N from the relation shown in Figure 14, and an estimated 3% statistical uncertainty in the LSF (see Section 6.3). For each combination of $\sigma_{H\alpha}$ and S/N, we draw 10^5 samples from the error distributions[27] for both σ_0 and ω_{PRE}, and compute the mean (σ_{rec}) and rms (ε_{rec}) of the 10^5 astrophysical velocity dispersions recovered following Equation (3).

The stellar velocity dispersions are significantly more complicated to model in detail as they are derived from a simultaneous fit across a wide range of different wavelengths.

[26] That is the errors determined from the fit covariance matrix (see, e.g., Press et al. 2007, Section 15.5) and the inverse variance vectors provided by the DRP.
[27] We test both an inverse gamma distribution (MacKay 2003, Section 24.1) and a simplified Gaussian distribution model with matched mode and rms. The differences between these distributions are negligible for high S/N, but become appreciable when the fractional error in σ_0 is $\gtrsim$10%.

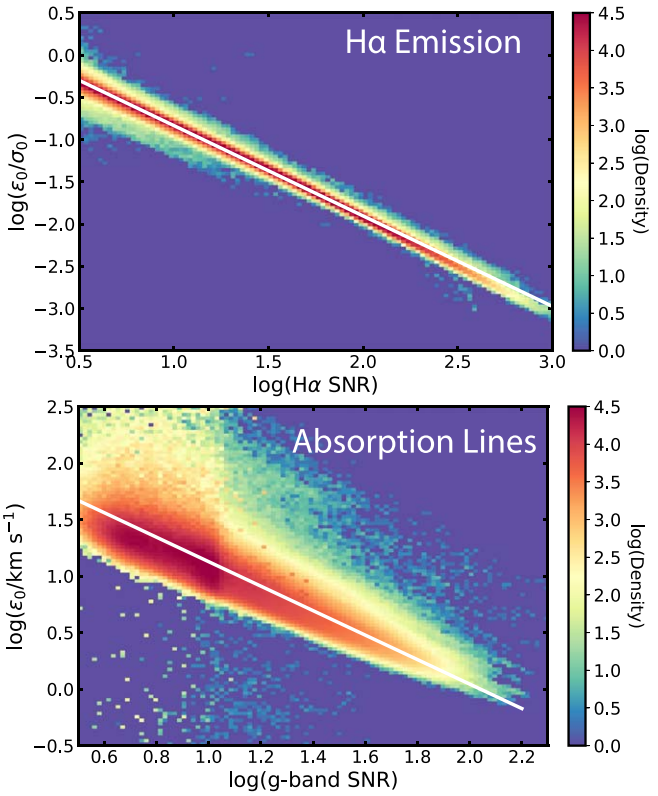

Figure 14. Top panel: fractional uncertainty ε_0/σ_0 in the observed emission-line width reported by the DAP as a function of emission-line S/N (colored density map). Bottom panel: uncertainty ε_0 in the stellar absorption-line measurements as a function of the g-band continuum S/N. In both panels, the white solid line indicates our functional fit to the relation. Note that the sharp feature around S/N = 10 for the stellar absorption-line measurements is an artifact of the Voronoi binning.

However, we obtain a rough estimate of their reliability by performing a similar series of Monte Carlo simulations using $\omega_{\rm PRE} = 74\,{\rm km\,s^{-1}}$ (i.e., an average value throughout the wavelength range of interest), combined with the observed error distribution in the observed stellar line widths.

As illustrated by Figure 15, the recovered line widths are most reliable at high S/N and high intrinsic astrophysical velocity dispersions, and the effective errors $\varepsilon_{\rm rec}$ in the recovered line width increase dramatically toward lower S/N. In addition, below the instrumental resolution, we note a systematic positive bias in the recovered velocity dispersions whose strength increases toward lower S/N and lower $\sigma_{\rm H\alpha}$ or σ_*. This expected behavior arises because of the asymmetric error distribution; namely, data points whose measured line widths (after application of mock measurement errors) are less than the instrumental line width produce imaginary astrophysical widths following Equations (3) or (4) and are thus preferentially lost from the sample.

In a per-spectrum sense, Figure 15 can be interpreted as giving the S/N cut required in order for the measurements to reach a given accuracy. In order to obtain velocity dispersions at $\sigma_{\rm H\alpha} = 20\,{\rm km\,s^{-1}}$ for which all data points have less than $1\,{\rm km\,s^{-1}}$ systematic error, for instance, the spaxel sample must be restricted to those with Hα S/N > 50, for which the typical statistical uncertainty $\varepsilon_{\rm rec}$ will be about $5\,{\rm km\,s^{-1}}$. Although more stringent cuts in S/N would produce samples with less systematic bias, the gain in such cases must be weighed against the dramatically decreased sample size at larger S/N thresholds.

We note that similar analyses have been performed for both the SAMI and CALIFA surveys, for which qualitatively similar trends are observed. Falcón-Barroso et al. (2017), for instance, note that the recovered stellar velocity dispersions in CALIFA are systematically larger than expected below $\sigma_* = 40\,{\rm km\,s^{-1}}$, at which point the random typical uncertainty in individual measurements is about 20%. Likewise, Fogarty et al. (2015) and van de Sande et al. (2017) find that systematic uncertainties in the instrumental resolution dominate the SAMI error budget for stellar velocity dispersions below $\sigma_* = 35\,{\rm km\,s^{-1}}$ and recommend a variety of quality cuts in both S/N and σ_* accordingly.

4.4. Consistency between Multiple Lines

In Belfiore et al. (2019, see their Figure 21) we noted that the astrophysical velocity dispersions computed from a variety of nebular emission lines were broadly consistent with those estimated using Hα. In Figure 16 we repeat this exercise for the MPL-10 data products and plot LOSVD ratios as a function of $\sigma_{\rm H\alpha}$ for all star-forming spaxels[28] in which both emission line are detected with S/N > 50. Given the large wavelength difference between [O II] and Hα, we additionally restrict [O II] observations to those with a Balmer decrement indicative of minimal dust attenuation ($f_{\rm H\alpha}/f_{\rm H\beta} < 3.5$).

We find that [O II], Hβ, [O III], [N II], and [S II] velocity dispersions all match $\sigma_{\rm H\alpha}$ to within a few percent, suggesting that there are no significant wavelength-dependent errors in the MaNGA LSF compared to the performance around Hα. Indeed, for $\sigma_{\rm H\alpha} > 30\,{\rm km\,s^{-1}}$, the small offsets that we see between the dispersions of different ions may be genuinely astrophysical in origin as the relative offset appears to be correlated with the ionization energy. The S^+ ion for instance has an ionization energy of 10.4 eV, and median $\sigma_{\rm [S\,II]}/\sigma_{\rm H\alpha} = 0.989$, while the H^+ and O^+ ions (both with 13.6 eV ionization energy) have median $\sigma_{\rm H\beta}/\sigma_{\rm H\alpha} = 1.004$ and $\sigma_{\rm [O\,II]}/\sigma_{\rm H\alpha} = 1.014$, respectively. Likewise, the N^+ and O^{++} ions have ionization energies of 14.5 and 35.2 eV, respectively, and median $\sigma_{\rm [N\,II]}/\sigma_{\rm H\alpha} = 1.027$ and $\sigma_{\rm [O\,III]}/\sigma_{\rm H\alpha} = 1.038$.

We note, however, that all four lines except [O III] show a ~10% turnup in their velocity dispersion relative to Hα at the lowest values of $\sigma_{\rm H\alpha} \sim 20\,{\rm km\,s^{-1}}$. If this were due to a systematic error in the LSF, it would imply a ~0.8% offset relative to Hα. However, this appears implausible given the small separation between Hα and [N II] in wavelength, and the well-sampled, well-behaved LSF in this range (see, e.g., Figure 9). Likewise, interpolation of the positivity bias from Figure 15 due to the differential S/N of Hα and the other emission lines suggests that this could account for at most a 1% deviation rather than the 10% observed.

The few-percent trends visible in Figure 16 may therefore be telling us more about the ionization structure of H II regions in the MaNGA galaxy sample rather than any low-level, systematic, and wavelength-dependent uncertainty in the spectral LSF of the instrument. Indeed, as we demonstrate in a forthcoming contribution (Law et al. 2020), typical gas-phase velocity dispersions can vary substantially depending on the

[28] Defined here as those with [O III]/Hβ versus [N II]/Hα line ratios below the relation defined by Kauffmann et al. (2003); see further discussion in Law et al. (2020).

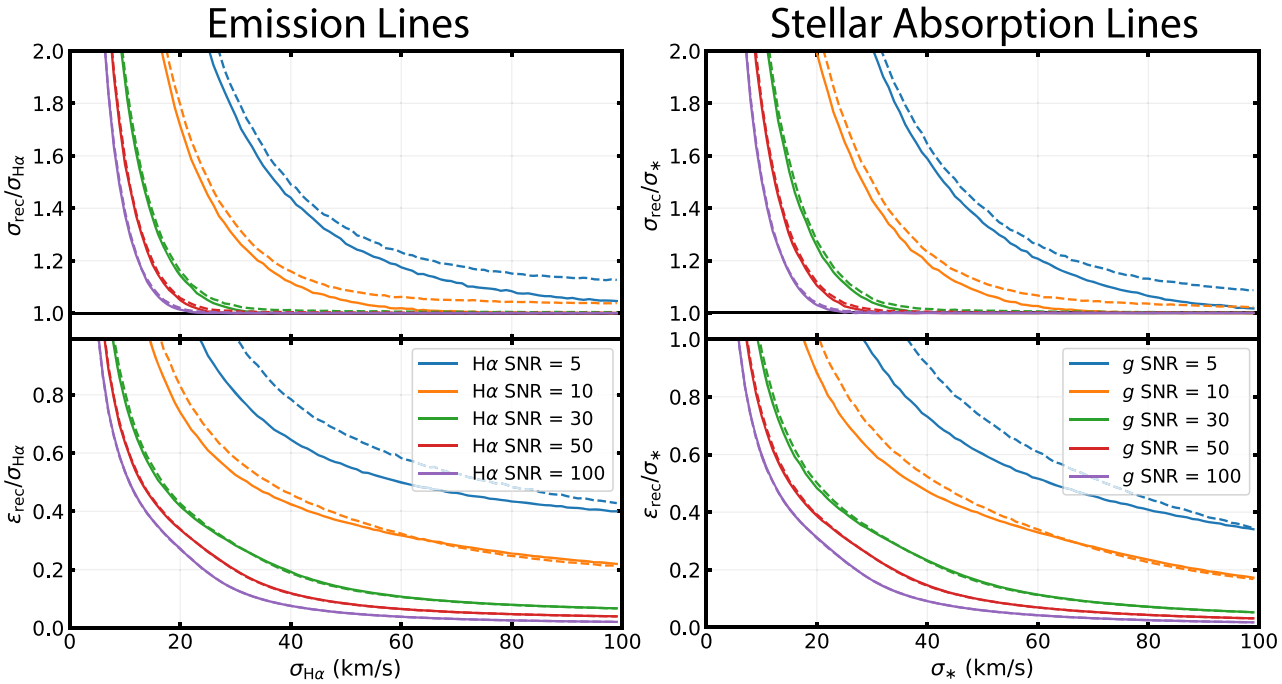

Figure 15. Top panels: sigma-clipped mean recovered velocity dispersion σ_{rec} as a function of the intrinsic astrophysical velocity dispersion for Monte Carlo simulations of emission lines and stellar absorption lines at a variety of S/Ns. Recovered velocity dispersions σ_{rec} are systematically larger than the astrophysical velocity dispersions ($\sigma_{H\alpha}$ and σ_*) at low dispersion due to the preferential loss of spaxels with observed line widths below the instrumental resolution from the sample. Bottom panels: typical fractional rms error $\varepsilon_{rec}/\sigma_{H\alpha}$ and $\varepsilon_{rec}/\sigma_*$ as a function of intrinsic dispersion for Monte Carlo simulations at a variety of S/Ns. In all panels, dashed lines represent simulations that adopt an inverse gamma error distribution, while solid lines represent simulations that adopt a simplified Gaussian distribution.

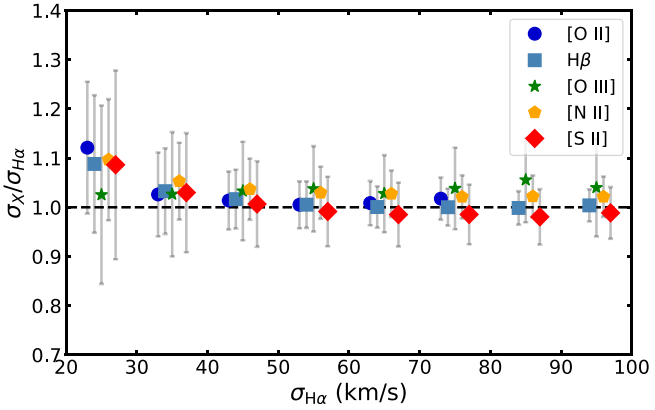

Figure 16. Ratio between Hα velocity dispersion and velocity dispersions of [O II] λ3727, Hβ [O III] λ5008, [N II] λ6584, and [S II] λ6717 as a function of $\sigma_{H\alpha}$. For each emission line, the sample is limited to star-forming spaxels for which both Hα and the other emission line are detected with S/N $>$ 50. Filled points show the sigma-clipped mean of the distribution while the error bars indicate the 1σ width of the observed distribution (uncertainties in the mean are smaller than the symbols).

selection method since these kinematics are strongly correlated with the ionization mechanism as traced by line ratios such as [N II]/Hα, [S II]/Hα, and [O III]/Hβ.

5. Beam Smearing

An additional consideration in the use of any velocity dispersions provided by the MaNGA DAP is the impact of beam smearing, or the effective broadening of velocity dispersions in a given spaxel by velocity gradients in the galaxy on scales comparable to the MaNGA point-spread function. The DAP does not correct for this effect, but given the typical MaNGA spatial resolution of 2.″5 FWHM (see, e.g., Figure 17 of Law et al. 2016), beam smearing can be significant, especially for edge-on high-mass galaxies at the high redshift end of the sample.

This problem is well known in the literature (e.g., Weiner et al. 2006; Epinat et al. 2010; Stott et al. 2016; Johnson et al. 2018; Varidel et al. 2019), and a variety of techniques have been developed to attempt to correct for it ranging in sophistication from simply ignoring the most-affected spaxels (e.g., Zhou et al. 2017) to quadrature subtraction of the local velocity gradient (Varidel et al. 2016; Oliva-Altamirano et al. 2018), Bayesian inference modeling (Varidel et al. 2019), and dynamical (e.g., Cappellari 2008) or 3D forward modeling of the observed data (e.g., Bouché et al. 2015; Bekiaris et al. 2016; Di Teodoro & Fraternali 2015). In the present study, we are bounded by our desire to make as robust a correction as possible, minimize loss of data, and also use a technique that can be practically applied to all ∼10,000 galaxies in the MaNGA sample without requiring substantial computing resources.[29] We therefore adopt a hybrid approach in which we correct for beam smearing estimated from a 3D model based on the observed velocity field of each galaxy, and additionally mask out from our analysis all spaxels within 4″ radius of the center of each galaxy for which the beam smearing correction will be most uncertain.

For each MaNGA galaxy, we first mask out all spaxels in the DAP Hα velocity map that have Hα S/N $<$ 3, or that have nonzero data quality bits set in the flux, velocity, or velocity-dispersion mask extensions. Next, we create a 3D model cube matched to the galaxy spaxels in which each non-masked

[29] At 450 hr per galaxy for instance, applying the BLOBBY3D bayesian mixture algorithm described by Varidel et al. (2019) to our data would require roughly 20 times the computing time required to generate the full DRP+DAP survey results from the raw observational data for MPL-10.

spaxel has a spectrum composed of a single emission line normalized to unity with a 1σ width 40 km s^{-1} and central wavelength shifted by the Doppler velocity given by the DAP velocity map.[30] This data cube is spatially convolved with the effective r-band PSF of the galaxy, effectively smearing together individual spectra in a manner that mimics the observed beam smearing. The resulting spectrum in each spaxel of the convolved cube is then fit with a Gaussian, and the initial 40 km s^{-1} line width is subtracted in quadrature from the measured width in order to determine a map of the effective beam smearing.

We illustrate this process in Figure 17, showing the observed velocity field and velocity-dispersion corrections for four example galaxies that span the range of MaNGA observations from nearby face-on objects (a best-case scenario) to distant edge-on objects (a worst-case scenario). As expected, beam smearing corrections vary significantly from ∼5–10 km s^{-1} at large radii for face-on galaxies such as 11944–12704 to 50 km s^{-1} or more in the centers of highly inclined galaxies such as 8996–12705. As illustrated by Figure 17, corrected velocity-dispersion maps in which the beam smearing contribution has been subtracted in quadrature from the observed values are relatively constant outside the central regions of MaNGA galaxies (peaking again in low-S/N regions toward the edges of the IFUs).

In addition to astrophysical processes, e.g., active galactic nuclei (AGNs) and spheroidal populations of old stars, that can produce broadened values of $\sigma_{H\alpha}$ in the central regions of our galaxies, these central peaks may also be due in part to limitations in our beam smearing correction. Strictly, in the approach described above, the true galaxy velocity field has been convolved with the observed PSF twice; once to produce the observed velocity map, and again during the model cube convolution. This effectively produces shallower velocity gradients in central regions of the galaxy, causing us to underestimate the true beam smearing in these regions. If we instead use a forward model (similar to that used by Westfall et al. 2014) to simultaneously fit the gas velocity and velocity-dispersion fields for the example galaxies shown in Figure 17, we derive beam smearing corrections for which the median absolute difference is just 2 km s^{-1} (i.e., insignificant when subtracted in quadrature), suggesting that outside the central regions, the difference between using the two models is small.[31] It may nonetheless be advisable for some science analyses to exclude spaxels within a 3″–4″ radius (i.e., ∼1.5 times the typical PSF FWHM; black circles in Figure 17) from consideration.

The effective beam smearing correction appropriate for stellar kinematics is more complicated to derive in detail, since the stellar kinematics provided by the DAP are derived from a simultaneous fit to multiple absorption lines at different wavelengths. However, we obtain a first-order estimate by repeating the same analysis as above and simply using the stellar velocity field in place of the ionized-gas velocity.

[30] The choice of 40 km s^{-1} is unimportant, and chosen to be small enough that broadening effects are easy to measure without producing double-peaked line profiles; the resulting beam smearing correction changes by just <1 km s^{-1} on average for any choice of model widths from 20 to 70 km s^{-1}. Likewise, the derived correction is insensitive to whether or not we rebin the velocity field to a smaller pixel scale prior to constructing the 3D model.

[31] Indeed, while the simple correction from the observed velocity map is imperfect in regions where the velocity gradient is extremely steep, it can nonetheless capture non-rotational kinematic effects missed by the method that assumes a fixed intrinsic form for the underlying velocity field.

6. External Assessment of the MaNGA Kinematics

6.1. Comparison to High-resolution Stellar Spectra

As a part of the MaStar stellar library program, we observed six bright stars (HD 284248, HD 37828, NGC 2682 108, NGC 6838 1009, HD 23924, and [W71b] 008-03) that had previously been observed at higher spectral resolution by X-Shooter. Since these stars have visual magnitudes $g = 6$–13 that are significantly brighter than typical MaNGA/MaStar targets, observations were made using custom 10–250 s exposures instead of the usual 900 s exposures. Since night skylines are too faint to be observed reliably in such short exposures, the DRP skips the skyline adjustment step (Section 3.3) for these observations and relies entirely upon the arc-lamp LSF solution.

We compared the final 1D spectra of these six stars produced by the DRP to high-resolution template spectra drawn from the X-Shooter Spectral Library (XSL; Chen et al. 2014). Spectra for HD 284248 and HD 37828 were taken from XSL DR1 (Chen et al. 2014) and have been processed with a unified resolution of $R = 7000$ across the wavelength range $\lambda =$ 3000–10185 Å, while the remaining four stars were taken from XSL DR2 (Gonneau et al. 2020) and have spectral resolution $R = 9793/11573$ in the MaNGA blue/red wavelength ranges, respectively. After converting the X-Shooter templates to the MaStar vacuum rest-frame wavelength solution and rebinning them to a constant pixel size of 30 km s^{-1}, we broke the spectra into 200–400 Å windows stepped every 100 Å and measured the effective spectral resolution based on a convolution of the high-resolution templates. After rejecting wavelength regions for which the MaStar and X-Shooter spectra do not match each other well (e.g., due to differences in the correction from telluric absorption bands), we plot the X-Shooter-derived LSF of the MaStar spectra against the DRP estimates in Figure 18.

As indicated by Figure 18, the effective spectral LSF derived from the X-Shooter spectra is generally in excellent agreement with the DRP-estimated LSF throughout the entire wavelength range. Although there are small systematic deviations for some of the stars (e.g., 12185–3703), these are generally within the uncertainty of the convolution technique given calibration differences between the spectra.

6.2. Comparison to the MILES Spectral Library

While Section 6.1 qualitatively suggested that the MaNGA LSF estimate was reasonable in the case of a single object with extant high-resolution data, the MaSTAR stellar spectral library provides an opportunity to test the pipeline-estimated LSF in a statistical manner as well. Barring unusual broadening due to stellar rotation and atmospheric features, the observed absorption-line width in a given MaSTAR spectrum should be similar to other stars of similar spectral type. Hence, comparing these MaSTAR spectra to those from a spectral template set with an established LSF we can test the robustness of the MaNGA LSF measurements.

For this test we conduct full-spectrum fitting of a large sample of MaSTAR spectra using the `pPXF` algorithm (Cappellari 2017) and the MILES-HC spectral template set (see Section 4.1, and Section 5 of Westfall et al. 2019). Since the LSF of the MILES stellar library is both well studied ($\omega_{MILES} = 2.54$ Å FWHM; Beifiori et al. 2011) and has slightly higher resolution than MaSTAR, a strong test of the accuracy of the MaNGA LSF estimate can be provided by

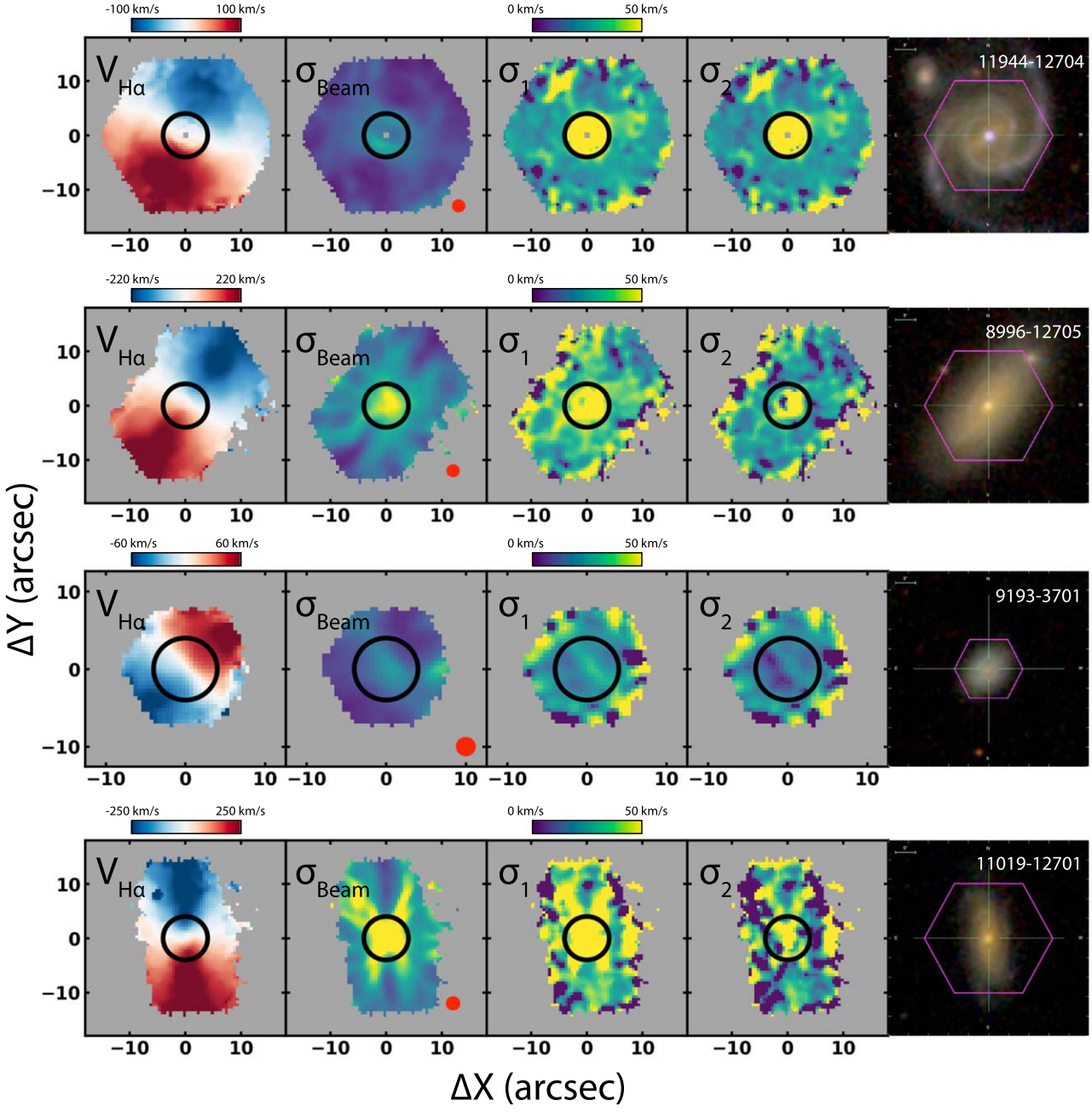

Figure 17. Beam smearing correction for four example galaxies selected to be widely representative of the MaNGA star-forming galaxy sample. Left to right, each panel shows the DAP Hα velocity map, our derived beam smearing correction $\sigma_{\rm beam}$, the gas velocity dispersion before (σ_1) and after (σ_2) application of the beam smearing correction, and a color image of the galaxy from SDSS imaging with the hexagonal IFU footprint overlaid in purple. The red circle in the second panel from the left indicates the FWHM of the MaNGA data, while the solid black circles in the four left-most panels illustrates the region with radius 4″ that we exclude from our future dispersion analyses. Examples are shown for a high-mass face-on galaxy (11944–12704; $\log(M_*/M_\odot) = 11.1$, $i = 36°$, $z = 0.069$, 1.5 R_e sample), a high-mass edge-on galaxy (8996–12705; $\log(M_*/M_\odot) = 10.8$, $i = 64°$, $z = 0.048$, 1.5 R_e sample), a low-mass face-on galaxy (9193–3701; $\log(M_*/M_\odot) = 9.2$, $i = 41°$, $z = 0.023$, 1.5 R_e sample), and a distant high-mass edge-on galaxy (11019–12701; $\log(M_*/M_\odot) = 11.1$, $i = 71°$, $z = 0.12$, 2.5 R_e sample).

comparing the broadening required to reproduce the MaSTAR spectra using the MILES-HC templates:

$$A = \sqrt{\omega_{\rm Fit}^2 - \omega_{\rm MILES}^2} \quad (5)$$

against the expected broadening factor based on $\omega_{\rm MILES}$ and the pipeline-reported LSF $\omega_{\rm PRE}$:

$$B = \sqrt{\omega_{\rm PRE}^2 - \omega_{\rm MILES}^2}. \quad (6)$$

In this test we compute A for a random sample of 5000 spectra from the MaSTAR sample of "Good Visit" spectra, which are single-visit observed spectra without extinction issues, having a median S/N per pixel greater than 15 and that pass a visual inspection for other quality problems (Yan et al. 2019). Due to the limited wavelength coverage of the MILES stellar library (and hence the MILES-HC templates), for this test we fit the MaSTAR spectra within a wavelength range of 3620–7400 Å. The full-spectrum fit is conducted using eight additive and multiplicative polynomials in order to account for issues of flux-calibration errors, reddening, template mismatch, etc. (see, e.g., Westfall et al. 2019).

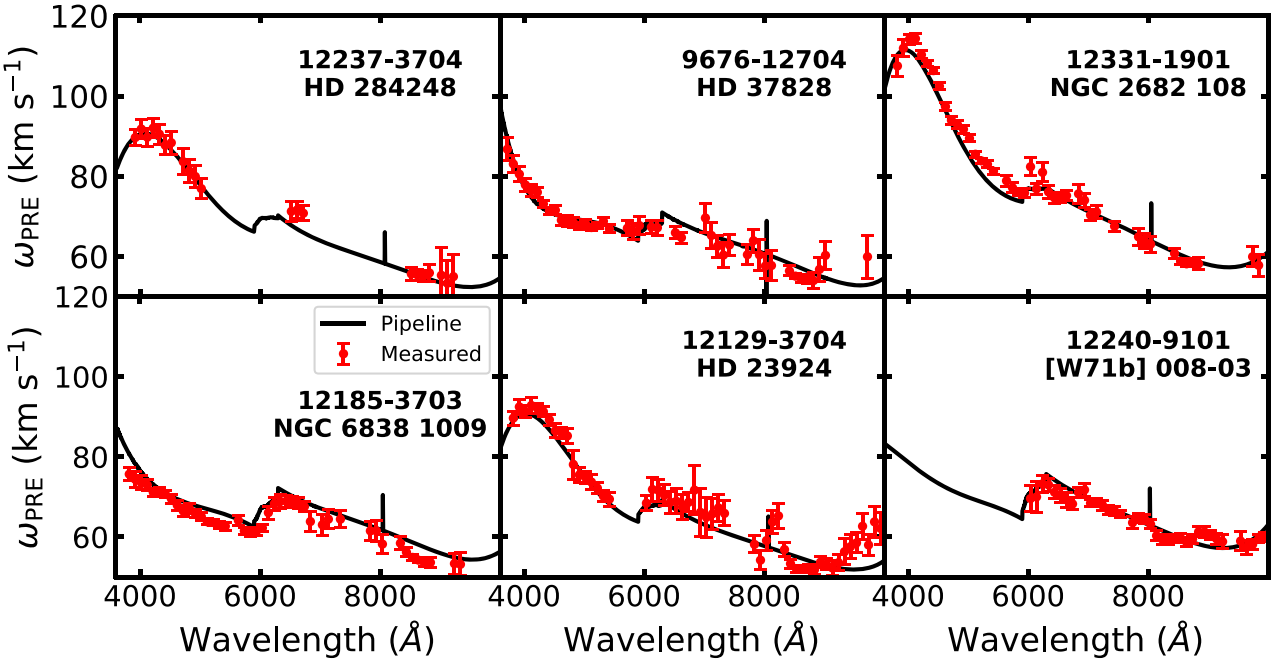

Figure 18. Internal pre-pixel DRP estimate of the spectral LSF for six bright MaStar targets (solid black lines) compared to empirical estimates derived via comparison of the MaStar spectra with previous $R = 7000$–$11{,}000$ X-Shooter spectra (red points, with 1σ uncertainties). Points are shown only for spectral bins in which the MaStar and convolved X-Shooter spectra are visibly well matched. No high-quality X-shooter spectra are available for short wavelengths in [W71b] 008-03.

Defining $\omega_{\rm Fit} = \omega_{\rm PRE}(1 + \delta)$ for some small δ, we can then write

$$\frac{A^2}{B^2} = \frac{\omega_{\rm PRE}^2(1+\delta)^2 - \omega_{\rm MILES}^2}{\omega_{\rm PRE}^2 - \omega_{\rm MILES}^2}. \quad (7)$$

Dropping terms $\mathcal{O}(\delta^2)$, we can solve Equation (7) for δ and find

$$\delta = \frac{\omega_{\rm PRE}^2 - \omega_{\rm MILES}^2}{2\omega_{\rm PRE}^2}\left(\frac{A^2}{B^2} - 1\right). \quad (8)$$

In Figure 19, we show the distribution of $\omega_{\rm PRE}\,/\omega_{\rm Fit} = \frac{1}{1+\delta}$ for the 5000 MaSTAR spectra in our sample. For MPL-9, we find that the distribution has a sigma-clipped mean of 0.97 and 1σ width of 0.05; i.e., suggesting that the the MPL-9 LSF is underestimated by about 3%. In contrast, for MPL-10, the distribution has a sigma-clipped mean of 0.99 and a 1σ width of 0.04, indicating that both the scatter of the distribution has decreased and the overall agreement between the pipeline and MILES estimates has improved to within 1%.[32] This result is broadly consistent with Figure 13, which found that the MPL-9 LSF estimate was ∼2%–3% narrower than the MPL-10 estimate in the wavelength range covered by the MILES library.

We note a few important caveats to this result however. First, the stellar absorption-line kinematics are the product of a convolution across a wide range of wavelengths across which the MaNGA LSF varies substantially. As such, the actual accuracy of the pipeline LSF at a given wavelength may be better or worse than 1%, depending on the effective weight of that wavelength range in driving the stellar population model fit. Likewise, our result is predicated upon the assumption that the MILES spectral resolution itself has <1% systematic error (statistical uncertainties are known to be ∼3%, see Falcón-Barroso et al. 2011), and that there are negligible systematic

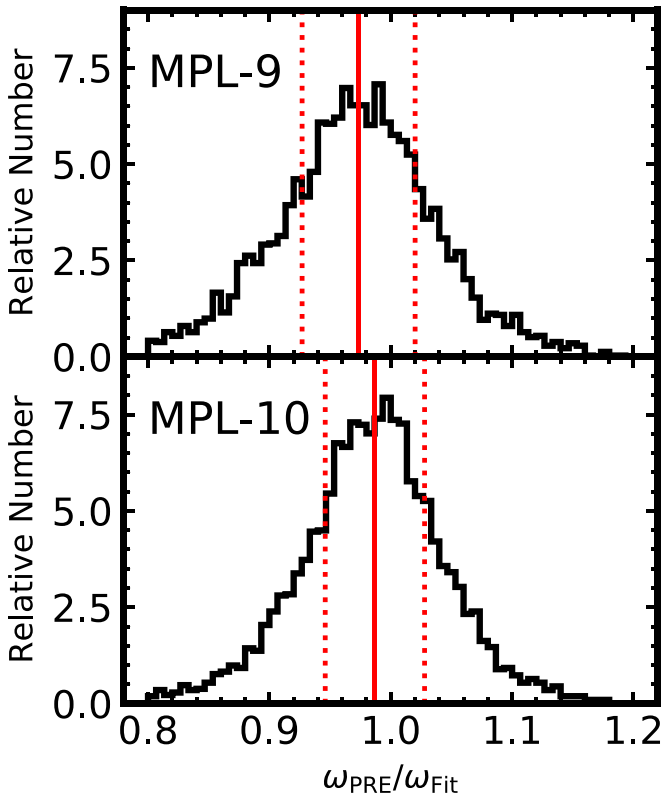

Figure 19. Ratio of the MaNGA LSF estimated from the pipeline ($\omega_{\rm PRE}$) vs. that derived from full spectral fitting with a series of MILES-HC templates ($\omega_{\rm Fit}$) for 5000 MaSTAR stellar spectra in MPL-9 and MPL-10. In each panel the solid red line indicates the sigma-clipped mean of the distribution, while the dotted red lines indicate the 1σ width of the distribution.

[32] Westfall et al. (2019, Figure 17) shows the results of a similar test, finding $A/B = 1.00$ for MPL-9, corresponding to $\omega_{\rm MPL-9}/\omega_{\rm Fit} = 1.00$. However, our previous analysis mistakenly used the post-pixel LSF estimate $\omega_{\rm POST}$ instead of $\omega_{\rm PRE}$ as should have been applied for a spectral convolution kernel, which approximately canceled out the error in the MPL-9 LSF (Figure 13).

Table 4
MaNGA DiskMass Overlap Sample

Plate-IFU	Name	Redshift[a]	Inclination[a]	Stellar mass[a] ($\log(M_*/M_\odot)$)
8566–12705	UGC 3997	0.0198	32°	10.1
8567–12701	UGC 4107	0.0117	24°	10.4
8569–12705[b]	UGC 463	0.0148	28°	10.8
8570–9101[b]	UGC 1087	0.0152	16°	10.3
8939–12704	UGC 4368	0.0129	36°	10.5
10494–12705	UGC 4380	0.0249	16°	10.8
10510–12704	UGC 6918	0.0037	30°	10.0

Notes.
[a] Derived from the NASA Sloan Atlas (Blanton et al. 2011) assuming $h = 0.7$ and a Chabrier (2003) IMF.
[b] Not observed prior to MPL-10.

differences due to template mismatch between MILES-HC and the MaSTAR sample.

6.3. Comparison to the DiskMass Survey

Perhaps the strongest possible test of the MaNGA LSF model for emission-line kinematics is to compare the derived galaxy-resolved velocity-dispersion profile $\sigma_{\mathrm{H}\alpha}$ in the face of LSF variations, beam smearing, and other factors against prior observations of the same galaxies from higher-resolution IFU observations. We therefore compared the MaNGA data against Hα observations[33] from the DiskMass survey (Bershady et al. 2010a, 2010b; Westfall et al. 2011, 2014; Martinsson et al. 2013), which used the SparsePak IFU (Bershady et al. 2004, 2005) on the 3.5 m WIYN telescope to obtain $R \sim 10{,}000$ ($\sigma_{\mathrm{inst}} = 12.7\,\mathrm{km\,s^{-1}}$) fiber spectroscopy of 176 spiral galaxies oriented nearly face-on to the line of sight. SparsePak fibers have 4.″7 diameters. As of MPL-10, MaNGA has observed seven galaxies in common with DiskMass (see Table 4), which can be identified via targeting bit 2^{16} in the ancillary target flag MANGA_TARGET3.

We compare the MaNGA and DiskMass samples by extracting kinematic data for all good-quality spaxels with S/N > 50 in the common region of overlap $4'' < r < 15''$. This radial cut is designed to exclude the central regions of the galaxies for which beam smearing is most significant and for which at least one galaxy (UGC 4368) exhibits Seyfert-I type AGN contributions to the Hα emission. In Figure 20 we plot a histogram[34] of the raw DiskMass and MaNGA measurements (i.e., uncorrected for beam smearing) for both MPL-9 and MPL-10. As illustrated in the left-hand panel, MPL-9 is appreciably biased with respect to the DiskMass data, peaking at $23.3\,\mathrm{km\,s^{-1}}$ instead of $16.7\,\mathrm{km\,s^{-1}}$, indicative of a 2.9% systematic underestimate in the LSF. In contrast, the MPL-10 histogram peaks at $18.2\,\mathrm{km\,s^{-1}}$, matching the DiskMass data to within a 0.6% systematic error in the LSF around Hα. If we account for the expected positivity bias in the MaNGA observations from Figure 15, this agreement improves further to about $17.4\,\mathrm{km\,s^{-1}}$, or about 0.3% systematic error in the LSF. Similarly, this level of agreement is largely insensitive to whether or not we apply a beam smearing correction to the MaNGA data; following the method described in Section 5, the corrected MPL-10 data matches the DiskMass observations to within 0.3%, and we obtain a comparable result if we instead estimate the beam smearing correction using a Bayesian forward model of a disk-like rotation curve.

We can also use the relative widths of the DiskMass and MaNGA MPL-10 distributions to assess the statistical error in individual estimates of the LSF. Assuming that the DiskMass histogram represents the true astrophysical range of $\sigma_{\mathrm{H}\alpha}$[35], we construct a Monte Carlo simulation with line width values drawn from the DiskMass distribution and convolve them with our median LSF of $68.5\,\mathrm{km\,s^{-1}}$ to create a mock set of observations. We then perturb these values by random errors combining the DAP-reported uncertainties in individual measurements (accounting for the plateau at high S/N discussed in Section 4.3) and some statistical uncertainty in the LSF. After subtracting the LSF from these perturbed values in quadrature, we compare the width of the simulated distribution to the MPL-10 observations. This exercise suggests that the statistical uncertainty in the LSF around Hα for a given spaxel is about 2%, corresponding to $1.4\,\mathrm{km\,s^{-1}}$ (i.e., comparable to the uncertainty in the measured line widths at high S/N).

6.4. Comparison to the SAMI Survey

As a final consistency check, we additionally compare the MaNGA data against similar observations obtained by the SAMI survey (Bryant et al. 2015) using the Sydney-AAO integral field spectrograph (Croom et al. 2012) on the Anglo-Australian Telescope. While SAMI has a similar spectral resolution to MaNGA in its blue arm, around Hα, SAMI has a spectral resolution $R \sim 4300$ delivering a 1σ LSF $\omega_{\mathrm{SAMI}} = 30\,\mathrm{km\,s^{-1}}$.

In MPL-10 we find that there are 74 targets observed in common between MaNGA and SAMI DR2 (Scott et al. 2018), and we select the 23 that have been observed with MaNGA's largest IFU bundle size (12 of which have significant Hα emission) for comparison. For each of these 12 galaxies, we extract the DAP kinematic measurements for all good-quality spaxels with S/N > 50 in the common radial range $3'' < r < 7.''5$, where the upper boundary is set by the size of the SAMI field coverage. Similarly, we extract all of the Hα kinematic measurements for these same galaxies provided by the SAMI DR2 public data products, introducing a limiting flux cut of $2 \times 10^{-17}\,\mathrm{erg\,s^{-1}\,cm^{-2}\,\AA^{-1}\,spaxel^{-1}}$, which visual inspection suggests selects a nearly identical range of spaxels for SAMI as the S/N > 50 cut does for MaNGA.

As we demonstrate in Figure 21 (top panels), despite the 2.3x higher spectral resolution of SAMI, the MaNGA MPL-10 Hα velocity dispersions are in excellent agreement with the values provided by SAMI DR2, with the centroids of the respective histograms matching each other to within $0.7\,\mathrm{km\,s^{-1}}$. As expected, the MPL-9 velocity dispersions are, in contrast, systematically too large by about $7\,\mathrm{km\,s^{-1}}$, consistent with our comparison against the DiskMass observations.

In addition to the statistical agreement between the MaNGA MPL-10 and SAMI DR2 velocity dispersions, we note also the excellent agreement in terms of the resolved spatial structures. In Figure 21 (bottom panels), we show an illustrative example

[33] Although the DiskMass survey observed [O III] as well, MaNGA does not detect [O III] from DiskMass galaxies at a sufficiently high S/N to enable a robust comparison.
[34] Strictly, we sum the normalized histograms of $\sigma_{\mathrm{H}\alpha}$ for each galaxy to ensure that no one galaxy dominates the distribution if it has more high-S/N spaxels than the others.
[35] Accounting for the median $1\,\mathrm{km\,s^{-1}}$ uncertainty in the DiskMass measurements has a negligible impact on our results.

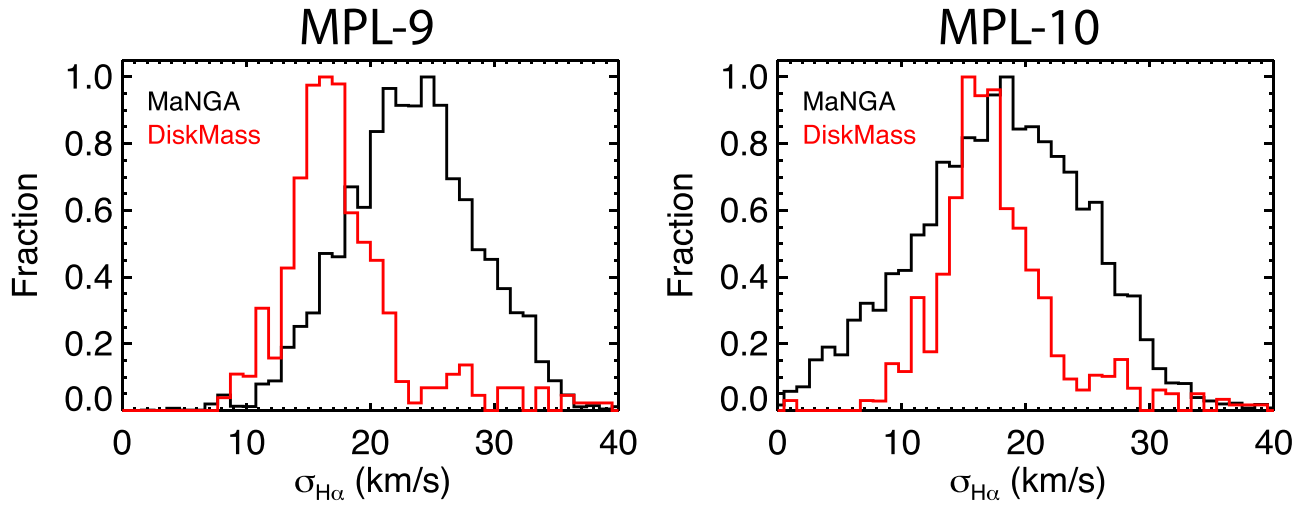

Figure 20. Distribution of Hα gas-phase velocity dispersions in the radius range $4'' < r < 15''$ for the seven galaxies observed in common with the DiskMass survey. The peak of the MPL-9 distribution is offset from the DiskMass distribution by about 7 km s^{-1}, while the peak of the MPL-10 distribution matches to within 1.5 km s^{-1}. Note that the DiskMass histograms differ slightly between panels as there are fewer galaxies in common with MPL-9 than with MPL-10.

of the Hα flux, velocity, and velocity-dispersion maps produced independently by the two surveys. The level of agreement between the two is exquisite, with even small and apparently insignificant features in the dispersion map appearing nearly identically in both sets of observations.

7. Summary

We have presented a major update to the MaNGA DRP that dramatically revises the treatment of the spectral LSF compared to both previous versions of the MaNGA DRP and the prior SDSS spectroscopic pipeline from which many original MaNGA routines were derived. After demonstrating that the LSF can be reliably parameterized as a Gaussian function with 1σ width ω (Figure 2), we showed in Section 3 that it is possible to use individual arc-lamp exposures in combination with unresolved night-sky emission features to construct a model of the LSF for all of the MaNGA fiber spectra. These models retain both pre-pixellized and post-pixellized measurements (i.e., measurements that either do or do not account for the contribution of the top-hat pixel response function to the effective LSF) and are carried through the pipeline accounting for various broadening terms to produce 3D LSF cubes corresponding to each of the MaNGA galaxy data cubes.

These LSF data cubes are then used by the MaNGA DAP (see Section 4) to produce kinematic maps that robustly subtract the instrumental contribution to the observed spectral line profiles. An important additional ingredient in such analyses that is not accounted for in the default DAP products is beam smearing, wherein the $\sim 2\farcs5$ FWHM MaNGA spatial PSF in the reconstructed data cubes can inflate the apparent line width from unresolved velocity gradients. As we demonstrated in Section 5, although typical beam smearing corrections in the radial range studied here (i.e., $r > 4''$) are small, they are nonetheless important at the few kilometers per second level and must be taken into account by science analyses that aim to study the cold disk regime around $\sigma_{H\alpha} = 10$–30 km s^{-1}.

Using Monte Carlo simulations, we demonstrated that the MaNGA DAP data products are reliable down to at least $\sigma_{H\alpha} = 20$ km s^{-1} for spaxels with S/N > 50 with a typical statistical uncertainty of 4–6 km s^{-1} and <1 km s^{-1} systematic bias (Figure 15). At lower $\sigma_{H\alpha}$ and/or lower S/N, the data exhibit increasingly large systematic biases toward larger values of $\sigma_{H\alpha}$ due to the asymmetric error distribution (i.e., spaxels whose measured line width scatters to below the nominal instrumental resolution are effectively lost from the sample). At other wavelengths, we showed in Section 4.4 that $\sigma_{[O\ II]}$, $\sigma_{H\beta}$, $\sigma_{[O\ III]}$, $\sigma_{[N\ II]}$, and $\sigma_{[S\ II]}$ are consistent with $\sigma_{H\alpha}$ to within 2% at $\sigma_{H\alpha} > 30$ km s^{-1}, with possible evidence for systematic variation as a function of ionization energy (Figure 16).

We have confirmed these findings by direct comparison of the MANGA data against higher-resolution external data. Qualitatively, we showed in Section 6.1 that the pipeline-estimated LSF is consistent to within the uncertainty with the LSF derived from comparing MaSTAR spectra of six bright stars against $R \sim 7000$–$11{,}000$ X-Shooter spectra. Quantitatively, we demonstrated in Section 6.2 that the overall pipeline LSF estimate is consistent at the 1% level with external assessments using the MILES stellar spectral library to perform full spectral fitting of 5000 stars drawn at random from the MaSTAR sample. Further, in Section 6.3 we demonstrated that the end-to-end derived MaNGA data products give Hα velocity dispersions peaking around $\sigma_{H\alpha} = 18.2$ km s^{-1} for seven galaxies in common with the $R \sim 11{,}000$ DiskMass IFU survey (Figure 20). Given the DiskMass result of $\sigma_{H\alpha} = 16.7$ km s^{-1}, this implies that the MaNGA LSF in the vicinity of Hα has a systematic uncertainty of $\leqslant$0.6% and a statistical uncertainty of 2%. Finally, we showed in Section 6.4 that the MaNGA Hα velocity dispersions are consistent with those derived from $R \sim 4300$ observations from the SAMI survey, with the distribution of values for a sample of 12 galaxies observed in common by the two surveys agreeing to within 0.7 km s^{-1}.

We therefore conclude that the MaNGA data products provided with internal release MPL-10 are sufficiently well calibrated to allow scientific analysis of the ionized-gas velocity dispersions down to about 20 km s^{-1} with sufficient care and attention to detail. Previous public MaNGA data releases (DR13, DR14, DR15) exhibit few-percent systematic biases in the instrumental LSF however (see Figure 13) that will complicate efforts to perform such analyses. Updated MaNGA products will be released publicly in DR17.

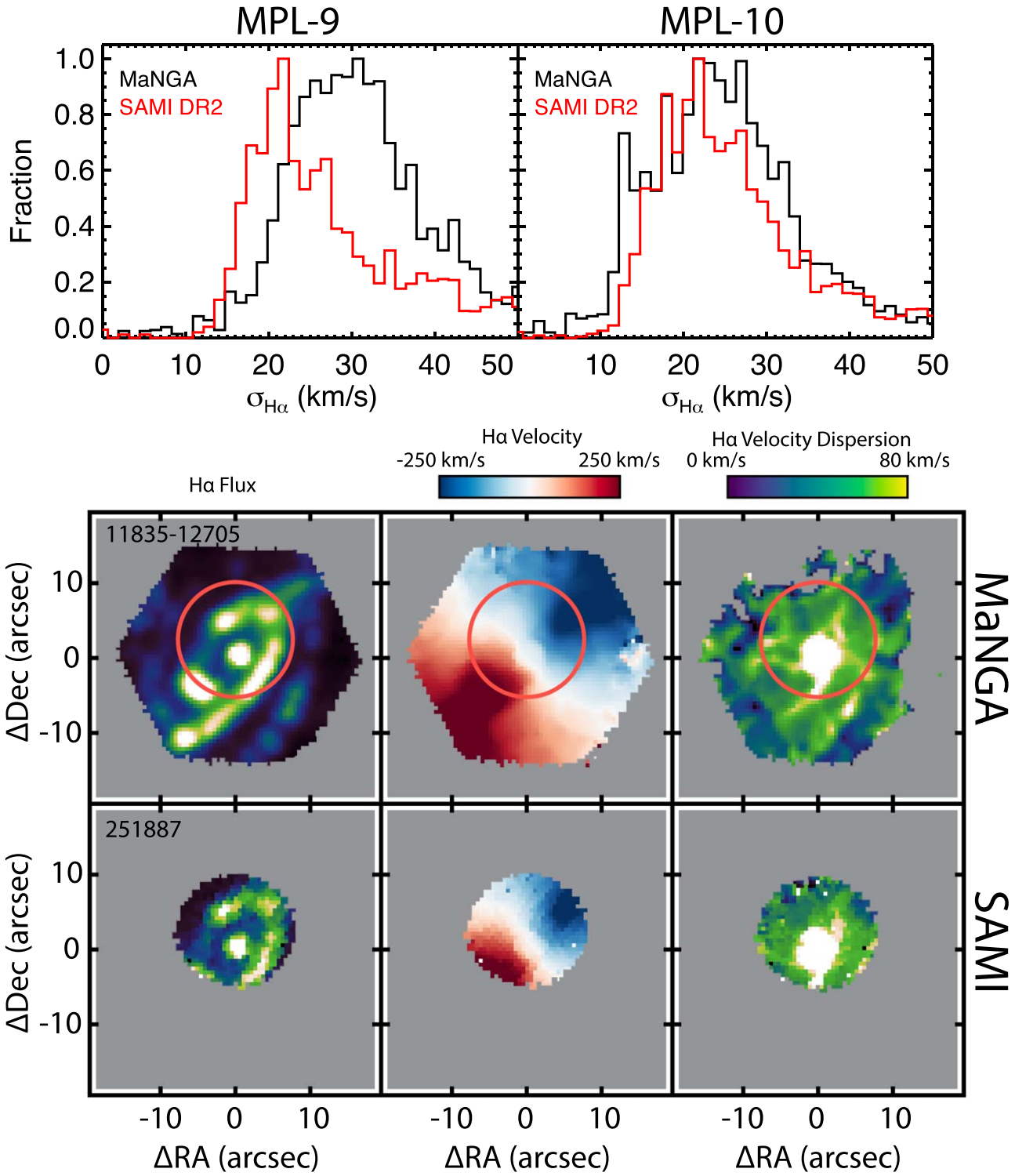

Figure 21. Top panels: distribution of Hα gas-phase velocity dispersions in the radius range $3'' < r < 7\farcs5$ for 12 galaxies observed in common with the SAMI survey. The peak of the MPL-9 distribution is offset from the SAMI DR2 distribution by about 7 km s^{-1}, while the peak of the MPL-10 distribution matches to within 0.7 km s^{-1}. SAMI DR2 histograms differ slightly between panels as there are fewer galaxies in common with MPL-9 than with MPL-10. Bottom panels: comparison of MaNGA and SAMI derived Hα flux, velocity, and velocity-dispersion maps for example galaxy 11835–12705 (GAMA ID 251887 in SAMI DR2). The red circles indicate the SAMI field of view. Note how even small irregularities in the velocity-dispersion maps are seen in both the MaNGA and the SAMI data.

D.R.L. appreciates productive discussions with Jeb Bailey, and constructive suggestions by the anonymous referee. R.Y. and D.L. acknowledge support by NSF AST-1715898. M.A.B. acknowledges NSF Awards AST-1517006 and AST-1814682.

Funding for the Sloan Digital Sky Survey IV has been provided by the Alfred P. Sloan Foundation, the U.S. Department of Energy Office of Science, and the Participating Institutions. SDSS-IV acknowledges support and resources from the Center for High-Performance Computing at the University of Utah. The SDSS website is www.sdss.org.

SDSS-IV is managed by the Astrophysical Research Consortium for the Participating Institutions of the SDSS

Collaboration including the Brazilian Participation Group, the Carnegie Institution for Science, Carnegie Mellon University, the Chilean Participation Group, the French Participation Group, Harvard-Smithsonian Center for Astrophysics, Instituto de Astrofísica de Canarias, The Johns Hopkins University, Kavli Institute for the Physics and Mathematics of the Universe (IPMU)/University of Tokyo, the Korean Participation Group, Lawrence Berkeley National Laboratory, Leibniz Institut für Astrophysik Potsdam (AIP), Max-Planck-Institut für Astronomie (MPIA Heidelberg), Max-Planck-Institut für Astrophysik (MPA Garching), Max-Planck-Institut für Extraterrestrische Physik (MPE), National Astronomical Observatories of China, New Mexico State University, New York University, University of Notre Dame, Observatário Nacional/MCTI, The Ohio State University, Pennsylvania State University, Shanghai Astronomical Observatory, United Kingdom Participation Group, Universidad Nacional Autónoma de México, University of Arizona, University of Colorado Boulder, University of Oxford, University of Portsmouth, University of Utah, University of Virginia, University of Washington, University of Wisconsin, Vanderbilt University, and Yale University.

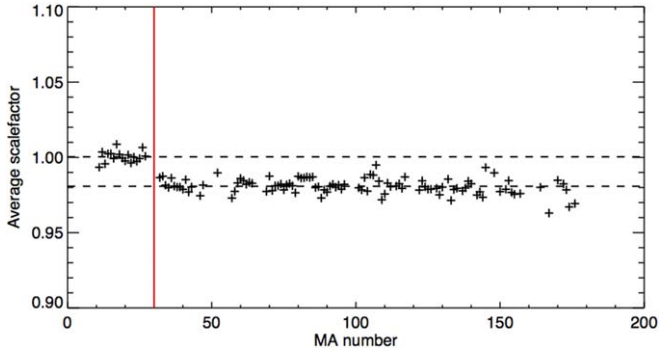

Figure A1. Fiber-bundle size scaling factor derived from comparing reconstructed MaNGA IFU data against SDSS broadband imaging as a function of the IFU harness identifier. Values shown represent averages over all galaxies observed with a given IFU. Note the 2% offset between empirical measurement and lab-derived scaling factors for harnesses in the MaNGA production run (MA part numbers greater than 30) compared to the commissioning harnesses. Gaps in the plotted points correspond to seven-fiber minibundles for which no scaling information is available.

Appendix A
Changes to MaNGA Fiber-bundle Metrology

The relative positions of individual fibers within each MaNGA IFU were measured in the lab to an accuracy of $\sim$0.3 μm, corresponding to 5 mas projected on the sky (Drory et al. 2015, their Section 4.5). However, the overall scale factor of the lab measurements was less well calibrated, resulting in a few-percent systematic uncertainty in the size of the IFU as a whole. With the advantage of years of on-sky observations, it has been possible to use MaNGA observations to empirically constrain any such systematic scale factor offsets and correct them in the survey metadata.

As discussed by Law et al. (2016, see their Section 8.2), the MaNGA DRP includes an "extended astrometry module" (EAM) that compares the galaxy images reconstructed from the IFU data to pre-existing SDSS broadband imaging photometry in each of the *griz* bandpasses. While the EAM is used automatically to determine any astrometric pointing or rotational offsets in individual exposures (due, e.g., to inaccuracies in the drilled plate hole locations, telescope pointing/guiding, and clocking biases from the tension of the IFU fibers within a given cartridge), it is also possible to adapt it to solve for any global scale factor offsets as well.

In Figure A1 we show the results of running the EAM with a global scaling term on all 6779 data cubes in MPL-8 using the original lab-based fiber metrology, and averaging over all galaxies observed with a given one of the $\sim$100 MaNGA science IFUs (17 science IFUs in each of six carts, with some additional spares swapped in over the lifetime of the survey). Although the optimal scale factors derived from individual galaxies can by noisy (particularly for relatively featureless galaxies), the average over many tens of galaxies per fiber bundle is extremely well behaved and shows that while the initial 30 IFUs built for MaNGA commissioning were correct to better than 1%, the remaining IFUs built during production had lab-measured scale factors that were systematically too large by 2%.

In v2.5.3 of the MaNGA DRP, we corrected the fiber-bundle metrology for this 2% scale error, along with an additional 0.5% in v2.7.1 based on an improved analysis permitted by the increasing number of galaxy observations. After applying these corrections, all scale factors derived by the EAM are consistent with unity to within 0.3%.

In practice, the impact of these changes between DR15 (v2.4.3) and MPL-10 are minimal and too small to detect for individual galaxies since a 2% scale factor change corresponds to a 0.″5 astrometric shift at the edges of the largest MaNGA fiber bundles. However, since the metrology of the calibration minibundles also changed, there was a corresponding change in the derived flux calibration. Since the bundles effectively got slightly smaller, the derived PSF shrank, corresponding to reduced throughput at fixed recovered values, causing a correction that produces data cubes whose fluxes are systematically brighter. In combination with the change from the O'Donnell (1994) to Fitzpatrick (1999) extinction curves, the typical galaxy thus became brighter by about 3% in v2.5.3 compared to v2.4.3.

Appendix B
Mitigation of the r1 "blowtorch" Artifact

Starting in Summer 2019, the r1 detector (one of the four BOSS CCDs) developed a persistent electronic artifact dubbed the "blowtorch" in which a region of extremely bright pixels produced a widespread glow that contaminated the lower-left region of the detector. Although multiple efforts were made to identify and fix the physical cause of the artifact, none of these efforts were wholly successful, and the MaNGA DRP therefore had to be modified to satisfactorily model and subtract this artifact from much of the final year of observational data.

As illustrated in Figure B1 (left column), the strength of the artifact was variable with time ranging from low (median signal $\leqslant$30 e- pixel^{-1} in the peak affected region), to moderate (median signal $\leqslant$1500 e- pixel^{-1}), to severe (up to about 9000 e- pixel^{-1}). Of the 1878 MaNGA science exposures from the final year of the survey, 157/1471/250 fall into each of these three categories, respectively.

As of DRP v3.0.1, for all frames in which the artifact is greater than 30 e- pixel^{-1} in strength, the DRP creates a model for the blowtorch component by first masking out all pixels near the fiber traces and then going row by row through the

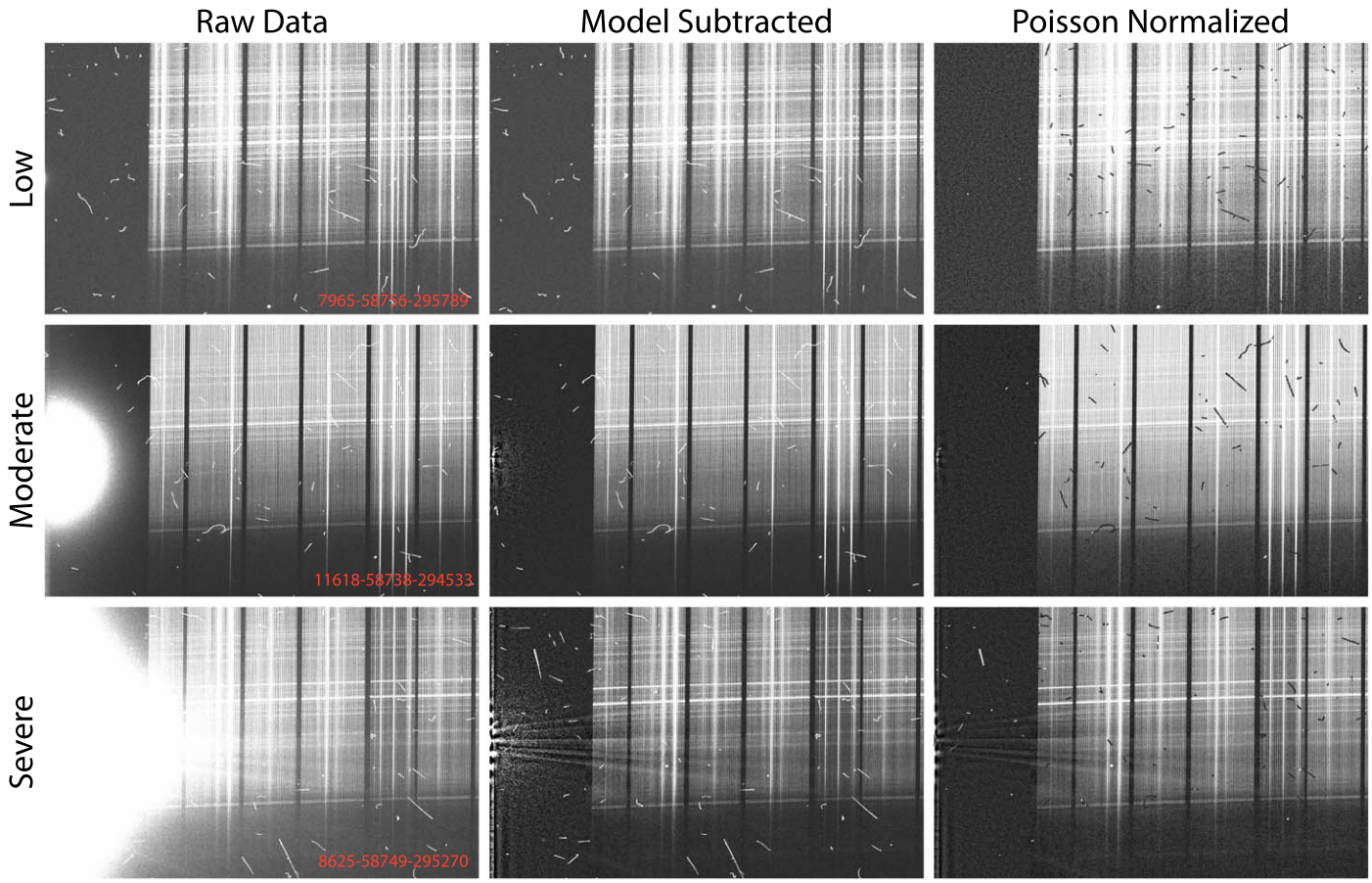

Figure B1. Left column: section of the raw detector images (after processing to remove quadrant-dependent bias, pixel flatfield, and overscan) for the BOSS r1 detector during the 2019–2020 survey year, illustrating the presence of an electronic artifact dubbed the "blowtorch." The strength of this artifact is variable, and examples are show for low (3 e- pixel^{-1}), moderate (1022 e- pixel^{-1}), and severe (9831 e- pixel^{-1}) cases. Red inset text gives the plate, MJD, and exposure number of the example frame. Middle column: residual detector images after subtraction of a spline-based model for the artifact. Right column: residual detector images after normalization by the expected Poisson noise based on the observed counts in each pixel. White and/or black streaks in each image are due to cosmic rays, which are automatically detected and masked by the DRP.

data, fitting a cubic spline function to the unmasked data points. This spline is constrained to have more closely spaced breakpoints in the region nearest to the artifact and widely spaced breakpoints at larger distance to avoid unphysical structure in the model far from the artifact. These row-by-row models are then fit with a second spline model running column-by-column in order to enforce smoothness of the final model in both detector dimensions.

Figure B1 (middle column) demonstrates that the residual detector image after subtraction of the spline model is relatively clean. Indeed, for moderate severity artifacts, the Poisson-normalized image (i.e., the residual count image divided by the shot noise) in Figure B1 (right column) shows that the subtraction leaves no artifacts in the region of the fiber traces other than a slightly higher noise. The DRP flags all data cubes with science exposures in this moderate category with the "BLOWTORCH" flag in the DRP3QUAL maskbit, although it is not expected to appreciably impact the science data quality.

Even in the most severe cases (Figure B1, bottom row) the subtraction does an excellent job, although the S/N degradation is significant (a factor ∼2–3), and there are residual spokes extending into the science data that were unable to be modeled. These spokes will manifest as unidentified emission features in the 6100–6300 Å range for the three IFUs on the left edge of the detector, and the DRP therefore flags all data cubes with science exposures in this category with the "SEVEREBT" and 'UNUSUAL' flags in DRP3QUAL. These data cubes are not included in the count of high-quality galaxy data cubes, although they will nonetheless be acceptable for the vast majority of science use cases.

ORCID iDs

David R. Law https://orcid.org/0000-0002-9402-186X
Kyle B. Westfall https://orcid.org/0000-0003-1809-6920
Matthew A. Bershady https://orcid.org/0000-0002-3131-4374
Michele Cappellari https://orcid.org/0000-0002-1283-8420
Renbin Yan https://orcid.org/0000-0003-1025-1711
Francesco Belfiore https://orcid.org/0000-0002-2545-5752
Dmitry Bizyaev https://orcid.org/0000-0002-3601-133X
Joel R. Brownstein https://orcid.org/0000-0002-8725-1069
Brian Cherinka https://orcid.org/0000-0002-4289-7923
Niv Drory https://orcid.org/0000-0002-7339-3170

References

Abolfathi, B., Aguado, D. S., Aguilar, G., et al. 2018, ApJS, 235, 42
Aguado, D. S., Ahumada, R., Almeida, A., et al. 2019, ApJS, 240, 23
Albareti, F. D., Allende Prieto, C., Almeida, A., et al. 2017, ApJS, 233, 25
Allen, J. T., Croom, S. M., Konstantopoulos, I. S., et al. 2015, MNRAS, 446, 1567
Beifiori, A., Maraston, C., Thomas, D., et al. 2011, A&A, 531, A109

Bekiaris, G., Glazebrook, K., Fluke, C. J., et al. 2016, MNRAS, 455, 754
Belfiore, F., Westfall, K. B., Schaefer, A., et al. 2019, AJ, 158, 160
Bershady, M. A., Andersen, D. R., Harker, J., et al. 2004, PASP, 116, 565
Bershady, M. A., Andersen, D. R., Verheijen, M. A. W., et al. 2005, ApJS, 156, 311
Bershady, M. A., Verheijen, M. A. W., Swaters, R. A., et al. 2010a, ApJ, 716, 198
Bershady, M. A., Verheijen, M. A. W., Swaters, R. A., et al. 2010b, ApJ, 716, 234
Blanton, M. R., Bershady, M. A., Abolfathi, B., et al. 2017, AJ, 154, 28
Blanton, M. R., Kazin, E., Muna, D., et al. 2011, AJ, 142, 31
Bohlin, R. C., Mészáros, S., Fleming, S. W., et al. 2017, AJ, 153, 234
Bouché, N., Carfantan, H., Schroetter, I., et al. 2015, AJ, 150, 92
Bruzual, A. G. 1983, ApJ, 273, 105
Bryant, J. J., Owers, M. S., Robotham, A. S. G., et al. 2015, MNRAS, 447, 2857
Bundy, K., Bershady, M. A., Law, D. R., et al. 2015, ApJ, 798, 7
Cappellari, M. 2008, MNRAS, 390, 71
Cappellari, M. 2017, MNRAS, 466, 798
Cappellari, M., & Copin, Y. 2003, MNRAS, 342, 345
Cappellari, M., & Emsellem, E. 2004, PASP, 116, 138
Chabrier, G. 2003, PASP, 115, 763
Chen, Y.-P., Trager, S. C., Peletier, R. F., et al. 2014, A&A, 565, A117
Cherinka, B., Andrews, B. H., Sánchez-Gallego, J., et al. 2019, AJ, 158, 74
Conroy, C., & van Dokkum, P. 2012, ApJ, 747, 69
Croom, S. M., Lawrence, J. S., Bland-Hawthorn, J., et al. 2012, MNRAS, 421, 872
Di Teodoro, E. M., & Fraternali, F. 2015, MNRAS, 451, 3021
Drory, N., MacDonald, N., Bershady, M. A., et al. 2015, AJ, 149, 77
Epinat, B., Amram, P., Balkowski, C., et al. 2010, MNRAS, 401, 2113
Falcón-Barroso, J., Lyubenova, M., van de Ven, G., et al. 2017, A&A, 597, A48
Falcón-Barroso, J., Sánchez-Blázquez, P., Vazdekis, A., et al. 2011, A&A, 532, A95
Fitzpatrick, E. L. 1999, PASP, 111, 63
Fogarty, L. M. R., Scott, N., Owers, M. S., et al. 2015, MNRAS, 454, 2050
Gonneau, A., Lyubenova, M., Lançon, A., et al. 2020, A&A, 634, A133
Gray, R. O., & Corbally, C. J. 1994, AJ, 107, 742
Gu, M., Conroy, C., Law, D., et al. 2018, ApJ, 859, 37
Gu, M., Conroy, C., Law, D., et al. 2020, ApJ, 894, 32
Gunn, J. E., Siegmund, W. A., Mannery, E. J., et al. 2006, AJ, 131, 2332
Johnson, H. L., Harrison, C. M., Swinbank, A. M., et al. 2018, MNRAS, 474, 5076
Kauffmann, G., Heckman, T. M., Tremonti, C., et al. 2003, MNRAS, 346, 1055
Law, D. R., Belfiore, F., Ji, X., et al. 2020, arXiv:2011.06012
Law, D. R., Cherinka, B., Yan, R., et al. 2016, AJ, 152, 83
Law, D. R., Steidel, C. C., Chen, Y., et al. 2018, ApJ, 866, 119
Law, D. R., Yan, R., Bershady, M. A., et al. 2015, AJ, 150, 19
MacKay, D. J. C. 2003, Information Theory, Inference, and Learning Algorithms (Cambridge: Cambridge Univ. Press)
Martinsson, T. P. K., Verheijen, M. A. W., Westfall, K. B., et al. 2013, A&A, 557, A131
O'Donnell, J. E. 1994, ApJ, 422, 158
Oliva-Altamirano, P., Fisher, D. B., Glazebrook, K., et al. 2018, MNRAS, 474, 522
Pace, Z. J., Tremonti, C., Chen, Y., et al. 2019, ApJ, 883, 82
Parikh, T., Thomas, D., Maraston, C., et al. 2018, MNRAS, 477, 3954
Press, W. H., Teukolsky, S. A., Vetterling, W. T., & Flannery, B. P. 2007, Numerical Recipes: The Art of Scientific Computing (3rd ed.; New York: Cambridge University Press)
Robertson, J. G. 2017, PASA, 34, e035
Sánchez, S. F., Pérez, E., Sánchez-Blázquez, P., et al. 2016, RMxAA, 52, 171
Sánchez-Blázquez, P., Peletier, R. F., Jiménez-Vicente, J., et al. 2006, MNRAS, 371, 703
Scott, N., van de Sande, J., Croom, S. M., et al. 2018, MNRAS, 481, 2299
Shetty, S., Bershady, M. A., Westfall, K. B., et al. 2020, ApJ, 901, 101
Smee, S. A., Gunn, J. E., Uomoto, A., et al. 2013, AJ, 146, 32
Stott, J. P., Swinbank, A. M., Johnson, H. L., et al. 2016, MNRAS, 457, 1888
Tabor, M., Merrifield, M., Aragón-Salamanca, A., et al. 2019, MNRAS, 485, 1546
van de Sande, J., Bland-Hawthorn, J., Fogarty, L. M. R., et al. 2017, ApJ, 835, 104
Varidel, M., Pracy, M., Croom, S., et al. 2016, PASA, 33, 6
Varidel, M. R., Croom, S. M., Lewis, G. F., et al. 2019, MNRAS, 485, 4024
Wake, D. A., Bundy, K., Diamond-Stanic, A. M., et al. 2017, AJ, 154, 86
Weiner, B. J., Willmer, C. N. A., Faber, S. M., et al. 2006, ApJ, 653, 1027
Westfall, K. B., Andersen, D. R., Bershady, M. A., et al. 2014, ApJ, 785, 43
Westfall, K. B., Bershady, M. A., & Verheijen, M. A. W. 2011, ApJS, 193, 21
Westfall, K. B., Cappellari, M., Bershady, M. A., et al. 2019, AJ, 158, 231
Worthey, G., & Ottaviani, D. L. 1997, ApJS, 111, 377
Yan, R., Bundy, K., Law, D. R., et al. 2016, AJ, 152, 197
Yan, R., Chen, Y., Lazarz, D., et al. 2019, ApJ, 883, 175
Yan, R., Tremonti, C., Bershady, M. A., et al. 2016, AJ, 151, 8
Zhou, L., Federrath, C., Yuan, T., et al. 2017, MNRAS, 470, 4573